

Closing the reactive carbon flux budget: Observations from dual mass spectrometers over a coniferous forest

Michael P. Vermeuel¹, Dylan B. Millet^{1*}, Delphine K. Farmer², Matson A. Pothier², Michael F. Link^{2^}, Mj Riches², Sara Williams², Lauren A. Garofalo²

¹ Department of Soil, Water, and Climate, University of Minnesota – Twin Cities, St. Paul, MN, USA

² Department of Chemistry, Colorado State University, Fort Collins, CO, USA

[^]now at Engineering Laboratory, National Institute of Standards and Technology, Gaithersburg, MD, USA

*Correspondence to D.B. Millet, dbm@umn.edu

Key Points

1. A small number of known organic compounds dominate the net and upward reactive carbon fluxes over a coniferous forest.
2. PTRMS captures VOCs controlling the net and upward fluxes, while ICIMS measures a range of important depositing species.
3. Far more VOCs contribute to the downward fluxes than are currently modeled, leading to a major sink underestimate.

Abstract

We use observations from dual high-resolution mass spectrometers to characterize ecosystem-atmosphere fluxes of reactive carbon across an extensive range of volatile organic compounds (VOCs) and test how well that exchange is represented in current chemical transport models. Measurements combined proton-transfer reaction mass spectrometry (PTRMS) and iodide chemical ionization mass spectrometry (ICIMS) over a Colorado pine forest; together, these techniques have been shown to capture the majority of ambient VOC abundance and reactivity. Total VOC mass and associated OH reactivity fluxes were dominated by emissions of 2-methyl-3-buten-2-ol, monoterpenes, and small oxygenated VOCs, with a small number of compounds detected by PTRMS driving the majority of both net and upward exchanges. Most of these dominant species are explicitly included in chemical models, and we find here that GEOS-Chem accurately simulates the net and upward VOC mass and OH reactivity fluxes under clear sky conditions. However, large upward terpene fluxes occurred during sustained rainfall, and these are not captured by the model. Far more species contributed to the downward fluxes than are explicitly modeled, leading to a major underestimation of this key sink of atmospheric reactive carbon. This model bias mainly reflects missing and underestimated concentrations of depositing species, though inaccurate deposition velocities also contribute. The deposition underestimate is particularly large for assumed isoprene oxidation products, organic acids, and nitrates—species that are primarily detected by ICIMS. Ecosystem-atmosphere fluxes of ozone reactivity were dominated by sesquiterpenes and monoterpenes, highlighting the importance of these species for predicting near-surface ozone, oxidants, and aerosols.

Plain Language Summary

Reactive carbon species in the atmosphere have a strong influence on air quality and climate and require accurate modeling to understand their global impacts. Natural ecosystems such as forests both emit and take up reactive carbon to and from the atmosphere, acting simultaneously as the largest source and an important sink of these species. We performed the most comprehensive measurements to date of this two-way reactive carbon exchange over a pine forest. We observed that the upward reactive carbon exchange was controlled by just a few known species and was much larger than the downward exchange, which was composed of far more species. We compared

the observations to chemical model predictions and found that the model accurately simulates the net reactive carbon exchange over this forest because the few species dominating that exchange are included in the model. However, the model does not adequately simulate the many depositing species, leading to a large underestimate for this sink of atmospheric reactive carbon.

1. Background

Surface-atmosphere exchange of volatile organic compounds (VOCs) plays a major role in modifying the chemical and physical properties of the atmosphere. In particular, the terrestrial biosphere is a major source of biogenic VOCs to the atmosphere ($\sim 1000 \text{ Tg C yr}^{-1}$) that is nearly an order of magnitude larger than the estimated anthropogenic source ($90\text{-}160 \text{ Tg C yr}^{-1}$) (Boucher et al., 2013; Glasius & Goldstein, 2016; Huang et al., 2017). Emission uncertainties for these biogenic VOCs frequently exceed 200% both globally and regionally (Sindelarova et al., 2014). Even for isoprene, the best-studied biogenic VOC, model disparities can reach a factor of 4 (Arneth et al., 2011). Developing an improved understanding of biosphere VOC emissions is thus an important science priority.

At the same time, terrestrial ecosystems are a primary depositional sink for oxygenated VOCs, which are compounds that can be directly emitted or formed in the atmosphere through VOC oxidation. Additional oxygenated VOC sinks include chemical reactions, wet scavenging, and condensation to form secondary organic aerosol (SOA) (Lary & Shallcross, 2000; Mellouki et al., 2015; Muller & Brasseur, 1999; Singh et al., 1995). Since oxygenated VOCs are ubiquitous and represent the majority of ambient reactive carbon (Bates et al., 2021; Chen et al., 2019; Heikes, 2002; Jacob et al., 2002; Millet et al., 2008, 2010, 2015), uncertainties in their dry deposition limit our understanding both of the overall VOC budget (Safieddine et al., 2017) and of the partitioning between reactive carbon loss pathways. For example, prior studies have shown that deposition uncertainties encompass a range that can change predicted oxygenated VOC and SOA concentrations by as much as 50% (Bessagnet et al., 2010; Nguyen et al., 2015).

With up to 10^5 different organic species thought to exist in the atmosphere (Goldstein & Galbally, 2007), there are open questions regarding the number of VOCs undergoing surface-atmosphere exchange (Park et al., 2013), the main environmental factors driving that exchange (Yáñez-Serrano et al., 2015), and the extent to which those factors are represented in current chemical transport models (CTMs; Millet et al., 2018). To date there have been few direct ecosystem-scale flux observations with comprehensive VOC coverage to address those questions. Park et al. (2013) performed detailed flux measurements over an orange orchard and detected 555 species contributing to the net VOC flux budget—with 10 commonly-known compounds making up 68% of the total flux. A recent study over a winter wheat field measured fluxes for 264 VOCs, with only four ubiquitous oxygenated VOCs accounting for 85% of total emissions (Loubet et al., 2022). A third study over a mixed temperate forest observed 377 VOCs with detectable surface-atmosphere exchange (Millet et al., 2018). While the GEOS-Chem CTM underestimated net fluxes by 40-60%, the exchange was dominated (90% on a carbon basis) by known VOCs included in the CTM—and isoprene alone represented >90% of the OH reactivity-weighted flux.

The aforementioned studies are limited by their reliance on proton-transfer reaction mass spectrometry (PTRMS) alone to characterize total ecosystem VOC fluxes. PTRMS measures a wide but incomplete suite of VOCs; the technique has been shown to capture a large portion of gas-phase VOC carbon (VOC-C) and associated OH reactivity over forests (Hunter et al., 2017), but it misses more oxidized VOCs, organic nitrates, organosulfur compounds, and other species that can undergo bidirectional surface-atmosphere exchange. Field deployable negative-ion chemical ionization mass spectrometry (CIMS) methods (e.g., using iodide, I^- ; acetate, CH_3COO^- ; or trifluoromethanolate, CF_3O^- ions) can detect molecules not present in the PTRMS spectrum (Beaver et al., 2012; Bertram et al., 2011; Lee et al., 2014; Mattila et al., 2018), thereby better constraining the speciation, direction, and magnitude of total VOC fluxes when paired with PTRMS measurements.

Here we present the most comprehensive ecosystem-scale VOC flux measurements to date, obtained by applying the eddy covariance (EC) technique to spectra collected simultaneously using dual high-resolution time-of-flight mass spectrometers (PTRMS and ICIMS). Measurements were

collected over a ponderosa pine plantation and provide a detailed and novel characterization of bidirectional fluxes across the two mass spectra encompassing hydrocarbons, low-to-mid molecular weight oxygenated VOCs, N-containing species, and halogenated species. Detected species are expected to cover the majority of gas-phase VOC-C and associated OH reactivity undergoing surface exchange (Hunter et al., 2017). We quantify the relative contributions of PTRMS- and ICIMS-detected species to the total net, upward, and downward VOC-C fluxes and interpret the combined observations with the GEOS-Chem CTM to test current understanding of VOC flux drivers and the importance of previously unknown or unmodeled compounds. We further determine the total OH and O₃ reactivity fluxes to better constrain the overall influence of two-way ecosystem VOC fluxes on atmospheric chemistry.

2. Methods

2.1 Measurement Site

The Flux Closure Study 2021 (FluCS 2021) took place from 06 August to 25 September 2021 at the Manitou Experimental Forest (39.1006° N, 105.0942° W, ~2370 m elevation) in the Colorado Front Range. Chemical and meteorological observations were made at the Manitou Experimental Forest Observatory (MEFO), a semi-arid mountainous site established by the National Center for Atmospheric Research (NCAR) in 2008 (Ortega et al., 2014). The site is surrounded by an open canopy of primarily ponderosa pine (~15 m height), shrubs, and grassland with a summertime leaf area index of ~1.2 m² m⁻² (Berkelhammer et al., 2016). The area is normally unpolluted but is at times impacted by surrounding cities (e.g., Colorado Springs), suburbs, and wildfires. The MEFO site has been previously used for EC studies of 2-methyl-3-buten-2-ol (232-MBO) and isoprene (Thomas Karl et al., 2014), small organic acids (Fulgham et al., 2019), and other oxygenated VOCs (Kaser et al., 2013a; S. Kim et al., 2010). Other detailed atmospheric chemistry studies at MEFO have primarily focused on reactive carbon abundance and chemistry (Karl et al., 2012; Kaser et al., 2013b; Link et al., 2021; Wolfe et al., 2014; Zhou et al., 2015).

FluCS 2021 included ambient observations of VOCs, NO_x, O₃, CO, and OH reactivity from a 28 m walk-up tower, along with HONO and HO_x radical measurements near the tower base. The

tower-based PTRMS and ICIMS measurements are described in the following section. VOC speciation was characterized via offline thermal desorption gas chromatography mass spectrometry (GC-MS) analysis of sorbent tubes that sampled ambient air as well as ponderosa pine and understory emissions using a portable photosynthesis system (PPS; LI-6800, LI-COR Biosciences) (Riches et al., 2020) (**S1.1**). A high-resolution aerosol mass spectrometer (HR-AMS; Aerodyne Research, Inc.) sampling 4.5 m above the ground at the instrument building measured submicron nonrefractory aerosol mass and composition (**S1.2**) (Canagaratna et al., 2015; DeCarlo et al., 2006).

Tower sampling employed custom built, identical PFA inlets (I.D. 0.375", length 45 m) held at 45 °C to minimize wall interactions and avoid water condensation. These inlets were installed at six heights (3.2, 6.9, 10.6, 14.6, 19.8, and 27.8 m) and oriented at 200° into the prevailing wind. 3D winds and temperature were recorded at 10 Hz from 6.9, 14.6, and 27.8 m using sonic anemometers (CSAT 3B, Campbell Scientific) collocated with the corresponding inlets. Inlets with sonic anemometers were mounted on 1.8 m booms to avoid wind modulation by the tower structure; remaining inlets were mounted on 0.9 m booms. A photosynthetically active radiation (PAR) sensor (MQ-100x, Apogee Instruments) positioned on the ground ~20 m in front of the sonic anemometers recorded half hourly photosynthetic photon flux densities (PPFD). **Fig. S1** summarizes the meteorological observations collected during FluCS 2021.

2.2 VOC measurements

VOCs were measured simultaneously using two high-resolution time-of-flight mass spectrometers housed in an air-conditioned trailer at the tower base. Both instruments employed the same custom-built automated sampling manifold to cycle through the six tower inlets every hour. The measurement sequence was offset between the two instruments and included 30 minutes of sampling from 27.8 m (for EC fluxes) followed by 5 minutes of sampling from each of the remaining inlets (for concentration gradients) and a 5 minute zero. Two rotary vane pumps (Model 1023, Gast Manufacturing) were used for sampling, with one dedicated to the 27.8 m inlet (35 standard liters per minute; SLPM) and one backing the remaining 5 inlets (10-15 SLPM each).

Continuous airflow was maintained through all six inlets to reduce surface adhesion. All wetted sampling surfaces upstream of the PTRMS and ICIMS were composed of PFA to avoid surface-catalyzed reactions of ambient compounds.

2.2.1 PTRMS Operation, Calibrations, and Data Processing

The PTRMS (PTR-QiTOF, Ionicon Analytik) time-of-flight analyzer collected ions (m/z 0-351) with a 33.2 μ s extraction period; the resulting spectra were coadded to obtain results at 10 Hz. The mass axis was continuously calibrated using peaks for water vapor (m/z 21.022, $H_3^{18}O^+$), acetone (m/z 59.049, $C_3H_7O^+$), and an internal diiodobenzene standard (m/z 203.943, $C_6H_5I^+$ and m/z 330.848, $C_6H_5I_2^+$). The drift tube was held at 2.9 mbar, 80 °C, and 740 V to maintain $E/N = 136$ Townsend (Td). The overall operating conditions led to sensitivities and mass resolutions of 2400 cps/ppb (cps counts per second) and 4200 $\Delta m/m$ for acetone, and of 850 cps/ppb and 4100 $\Delta m/m$ for β -pinene. PTRMS subsampling details are outlined in **S1.3**.

The PTRMS was zeroed for 5 minutes hourly by passing sampled air through a platinum bead catalyst (3.2 mm diameter; Shimadzu Corp.) heated to 400 °C. Calibrations were performed once daily for 45 minutes between 00:00-03:00 Mountain Daylight Time (MDT) while the PTRMS was sampling from 27.8 m, with uninterrupted sampling of nocturnal gradients on the other inlets. Four-point calibration curves were collected for 27 VOCs via dynamic dilution of compressed ppm-level gas-phase standards into zero air (Apel-Reimer Environmental; **Table S1**). Laboratory calibrations were performed post-study for individual monoterpene (MT) isomers and for oxygenated terpenoids using aspirated cyclohexane solutions (**S2.1**; **Fig. S2-S3**). Formaldehyde (HCHO) calibrations were also performed post-study using a compressed standard, and the HCHO signal was corrected for methanol interference (**S2.2**; **Fig. S4**). Ambient isoprene concentrations and fluxes were derived by removing the 232-MBO contribution to measured signals at m/z 69.069 (**S2.2**). All signals were normalized to 2×10^5 cps of $H_3^{18}O^+$.

The total sesquiterpene (Σ SQT; $C_{15}H_{25}^+$, m/z 205.195) signal was calibrated on the last study day using a compressed β -caryophyllene standard. We apply the β -pinene sensitivity to the total monoterpene (Σ MT; $C_{10}H_{17}^+$, m/z 137.133) signal as this compound had the median sensitivity across all MT isomers identified with the offline GC-MS measurements. Sensitivities for other MT isomers were within 30% of β -pinene (**Fig. S2**). Uncalibrated VOCs employ the measured sensitivity for methacrolein (~ 1100 ncps/ppb), which had the median sensitivity and humidity dependence across all calibrated compounds. We then apply the second lowest and highest measured sensitivities for all VOCs (275 – 3000 ncps ppb^{-1}) to derive lower and upper uncertainty bounds for the sum of uncalibrated species.

Humidity corrections were derived on the last study day by diluting VOC standards into zero air with varying water vapor concentrations (LI-610 Portable Dew Point Generator, LI-COR Biosciences). Water vapor concentrations were determined from the ratio of $H_2O^+H_3O^+$ (m/z 37.028) to $H_3^{18}O^+$, scaled by isotopic abundance: $(H_2O^+H_3O^+)/ (500 \times H_3^{18}O^+)$. Values of this ratio ranged from 0.003 – 0.05 during the study. Calibration curves were collected at dew points ranging from -10 to 15 °C ($(H_2O^+H_3O^+)/ (500 \times H_3^{18}O^+) = 0.002 - 0.2$), with the resulting sensitivity vs. water signal fits used to humidity-correct the field data. These corrections led to only modest (typically $<15\%$) changes in the derived calibrations.

Peak fitting and integration were performed using the Ionicon Data Analyzer v 1.0.0.2 (IDA; Ionicon Analytik) (Müller et al., 2013). A custom table of 1340 peaks for m/z 13–351 was generated from this dataset, with 56 days of continuous 10 Hz data then fitted and integrated in one week on a standard workstation. Of the 1340 ions, 776 species were identified using PTRwid (Holzinger, 2015) and the molecular formula assignment workflow used in Millet et al. (2018). All subsequent data processing was performed in MATLAB (R2021a, MathWorks).

2.2.2 ICIMS Operation, Calibrations, and Data Processing

The ICIMS (Bertram et al., 2011; Brophy & Farmer, 2015) sampled at 5 Hz resolution, measuring ions of mass range m/z 2-491 with an extraction frequency of 40 μ s. During measurement, the instrument pulls 1.9 SLPM of ambient air into the ion molecule reactor (IMR) where it mixed with 1.3 SLPM of humidified ultra-high N_2 humidified to 85% (to reduce the instrument water dependence) and 1.0 SLPM of I^- ions in ultrahigh purity N_2 , both introduced directly into the IMR. The IMR was held at ambient temperature and 100 mbar pressure. The ICIMS was zeroed for one minute every hour via N_2 overflow, followed by external standard calibrations of C_1 - C_5 alkanolic acids via permeation tube over the subsequent four minutes. Tofware (v3.2.0, Aerodyne Research, Inc.) fit the mass spectra to the 578 selected ions, and integrated peak areas. The final reported peaklist (485 analyte ions) used for the data analysis herein was limited to include only organic compounds containing C, H, N, and O. We normalize all ICIMS signal to the average sum of I^- and $I \cdot H_2O^-$ during instrument zeros ($\sim 1.4 \times 10^6$ cps). The mass resolution and sensitivity for formic acid (CH_2O_2) were 3500 $\Delta m/m$ and 7.29 ncps ppt⁻¹, respectively. We estimate sensitivities for uncalibrated species using the log-linear dependence of instrument sensitivity on the gradient in voltages (dV) between adjacent ion optics within the ICIMS that controls collisionally-induced dissociation of I^- adducts (Lopez-Hilfiker et al., 2015). We determined the half-maximum of a sigmoidal fit of dV vs. analyte signal (dV_{50}) for a suite of calibrants to quantify the relationship between sensitivity and dV_{50} (**Fig. S5**), which was then applied to field-determined dV_{50} values for uncalibrated species across the ICIMS spectrum (**S1.4**) (Bi et al., 2021; Iyer et al., 2016; Lopez-Hilfiker et al., 2014; Mattila et al., 2020). Errors in sigmoidal fits were propagated to derive sensitivity uncertainties for uncalibrated ICIMS species.

There was some overlap in species coverage between the PTRMS and ICIMS, including for several organic acids; in these cases, results were employed from a single instrument based on superior flux signal-to-noise and/or availability of in-field calibrations.

2.4 Flux calculations

EC fluxes were calculated from the covariance of concentration (X) with vertical wind (w) for an ensemble of n measurements (Stull, 1988) within a 30-minute period:

$$F_C = \overline{w'X'} = \frac{1}{n} \sum_{i=1}^n (w_i - \bar{w})(X_i - \bar{X}) \quad (\text{E1})$$

Fluxes were derived based on the native PTRMS and ICIMS sampling frequencies of 10- and 5-Hz, respectively. Concentrations and winds were first despiked using the median absolute deviation method (Mauder et al., 2013) and detrended by subtracting a linear fit to each 30-minute signal time series. Winds underwent double rotation so that $\bar{w} = 0$ for each averaging period (X. Lee et al., 2005). The time lag between the sonic wind measurements and the corresponding VOC detection within the mass spectrometer was quantified from the maximum w - X cross-covariance. Lag times derived in this way for Σ MT and formic acid (HCOOH) were employed for all PTRMS and ICIMS compounds, respectively (**Fig. S6**), due to the high flux signal-to-noise in each case.

Flux uncertainties were determined for each averaging period as $1.96\times$ the standard deviation of the outer 30 points within a 600-point lag time window centered around the peak in w - X cross-covariance. The resulting flux uncertainties averaged 16%, 21%, and 8% for 232-MBO, Σ MT, and HCOOH, respectively. Species whose mean fluxes were lower than their uncertainty calculated in this way were removed from the following analyses. Sensitivity tests described later assess how the inclusion versus exclusion of these compounds affects our overall findings. Additional recommended EC filtering criteria were applied based on wind shear and stationarity (**S3**) (Foken & Wichura, 1996).

Figure S7 shows examples of frequency-normalized cospectra for VOCs measured by PTRMS and by ICIMS as well as for sensible heat. High frequency attenuation through the sampling line was estimated for each VOC using the empirical model of Horst (1997) (**S4**), resulting in cumulative corrections of 8.2% and 43%, respectively, for the total upward and downward fluxes, and a 5.5% correction for the net flux (**Fig. S8**).

2.5 Model runs

Model simulations for the study period were performed using GEOS-Chem v13.3.0 (<https://geos-chem.org/>). The model uses assimilated meteorological data (Goddard Earth Observation System

Forward Processing product; GEOS-FP) from the NASA Global Modeling and Assimilation Office (GMAO), which have native horizontal resolution of $0.25^\circ \times 0.3125^\circ$, 72 vertical layers, 3-h temporal resolution for 3-D meteorological parameters, and 1-h resolution for surface quantities and mixing depths. We performed a nested, full-chemistry simulation at $0.25^\circ \times 0.3125^\circ$ using the FlexGrid functionality for 06 July to 01 October 2021 within a custom domain surrounding MEFO ($\pm 3^\circ$ latitude and longitude). Boundary conditions were taken from a $2^\circ \times 2.5^\circ$ global model run for the same time period that was itself initialized using output from a year-long global simulation at $4^\circ \times 5^\circ$. Nested simulations employed 5 and 10 min timesteps for transport and chemistry, respectively, while global simulations used 15 and 30 min timesteps (Philip et al., 2016).

The full-chemistry GEOS-Chem chemical mechanism used here features comprehensive HO_x - NO_x - O_x -VOC-Br-Cl-I chemistry coupled to aerosols and incorporates the most recent JPL/IUPAC recommendations. GEOS-Chem v13 also incorporates recent chemical updates for isoprene oxidation (Bates & Jacob, 2019), small oxygenated VOCs (Bates et al., 2021; Chen et al., 2019), halogens (Wang et al., 2019), and small alkyl nitrates (Fisher et al., 2018). For the present analysis we added simplified oxidation schemes for 232-MBO, ΣSQT , and $>\text{C}_2$ organic acids (lumped as RCOOH and treated as propanoic acid) to the chemical mechanism (**Table S2**), with RCOOH dry deposition also included (**Table S3**) using a Henry's law constant for propanoic acid from Sander (2015). Rate coefficients for the updated mechanisms are taken from the Master Chemical Mechanism (Saunders et al., 2003) and product yields from published laboratory studies (Fantechi et al., 1998; Ferronato et al., 1998).

Land cover in the $0.25^\circ \times 0.3125^\circ$ model grid cell containing the MEFO site is heterogenous, with 6 Community Land Model (CLM) classifications and cropland plus bare ground accounting for 46% of the total area. This is not representative of the $1 \times 1 \text{ km}^2$ measurement footprint, which primarily consists of ponderosa pine, grass, and shrubs (**Fig S9-S10**). We therefore modified the model land cover and leaf area to more realistically reflect the MEFO site as described in **S5** (Byrne et al., 2005; Guenther et al., 2006; Olson et al., 2001).

Model emissions use the Harmonized Emissions Component module version v3 (HEMCO v3) (Lin et al., 2021), with biogenic emissions from terrestrial plants computed online using the Model of Emissions of Gases from Nature (Guenther et al., 2012) as implemented in GEOS-Chem by Hu et al. (2015). For simulations here we implemented 232-MBO and Σ SQT emissions and updated the plant species-specific basal emissions for all VOC to the latest available MEGAN values (MEGAN v3.2; Guenther et al., 2020) within the nested domain. Global anthropogenic emissions are from the Community Emissions Data Systems (CEDS, year-2019) inventory (Hoesly et al., 2018) and biomass burning emissions from the Global Fire Emissions Database v4 (GFED4, year-2019) (Giglio et al., 2013).

In analyses that follow, cumulative model fluxes are calculated by summing the simulated emissions, dry deposition, and net chemical production/loss scaled to the height of the first model layer (**Fig. S11**). The net chemical production/loss is then the average of two limiting cases where either all or none of the production/loss in this grid cell occurs below our sensor.

3. Results and Discussion

3.1 Contributions to VOC carbon flux

Many species contributed to the measured VOC-C fluxes over the sampled ecosystem. Of the 744 PTRMS and 485 ICIMS ions identified as VOCs, 230 and 85 had detectable fluxes, respectively, based on an S/N threshold of 1.96. This drops to 65 (PTRMS) and 25 (ICIMS) when instead using S/N=3 (**Figure S8**). **Figure 1** shows the contribution of individual ions to the total detected VOC-C mass flux. Net fluxes were partitioned into upward and downward components based on the exchange direction for each molecule and averaging period (**Figure 1a**), allowing bidirectional ions to contribute to both upward and downward fractions. **Table S4** shows the top ten contributors to upward and downward VOC-C fluxes, as well as to the reactivity fluxes discussed later.

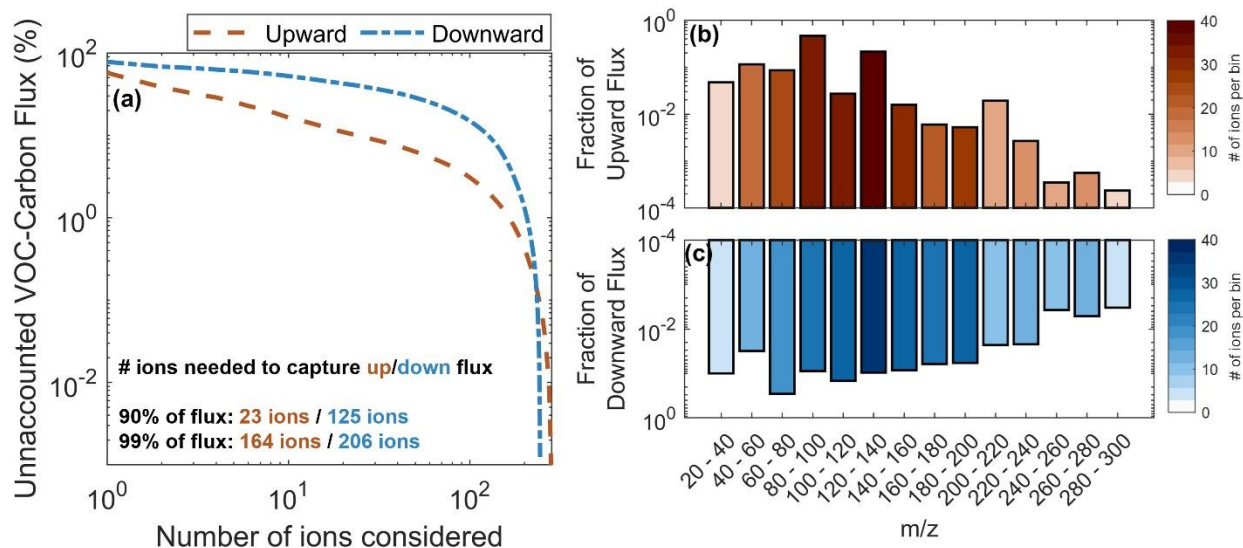


Figure 1: Summary of observed VOC ions undergoing ecosystem-atmosphere exchange. a) Percentage of unaccounted VOC-C upward (orange) and downward (blue) fluxes as a function of the number of ions considered. b) Fractional ion contributions to the total observed upward (top, orange) and downward (bottom, blue) fluxes. Each bin is colored by the number of ions encompassed. 315 total ions with detectable flux are included.

Measured upward VOC-C fluxes at MEFO arise from 283 individual ions, but a large majority of the mass comes from a small number of known species that are commonly simulated in CTMs. 232-MBO (43%) and Σ MT (19%) make up ~60% of the cumulative upward mass flux, with ethanol (C_2H_5OH), methanol (CH_3OH), hydroxyacetone ($C_3H_6O_2$), and isoprene (C_5H_8) contributing an additional 15%. In all, only 23 species account for 90% of the upward VOC-C flux, and these are exclusively hydrocarbons or oxygenated VOC with 3 or fewer oxygen atoms ($no \leq 3$). Sesquiterpenes make up 1.7% of the observed upward flux on a carbon basis, but as will be seen later, they make a much larger contribution to the reactivity fluxes. These observations represent one of just a few reported canopy-scale flux datasets for Σ SQT (Fischer et al., 2021; Vermeuel et al., 2022). The remaining 10% of the upward VOC-C flux beyond the 23 dominant compounds is more diverse, with 164 ions needed to capture 99% of the total.

245 total ions had detectable downward fluxes during the campaign. Of these, 125 ions accounted for 90% of the flux—compared to just 23 for the upward fluxes. The two largest contributors to the cumulative downward VOC-C flux were $C_3H_6O_2$ (22%) and $HCHO$ (9.8%). Other key

contributors included acetic acid ($\text{C}_2\text{H}_4\text{O}_2$), other likely organic acids (e.g., succinic acid, $\text{C}_4\text{H}_6\text{O}_4$; lactic acid, $\text{C}_3\text{H}_6\text{O}_3$; pyruvic acid, $\text{C}_3\text{H}_4\text{O}_3$), anhydrides (maleic anhydride, $\text{C}_2\text{H}_4\text{O}_3$; acetic anhydride, $\text{C}_4\text{H}_6\text{O}_3$), and isoprene oxidation products (ISOPOOH/IEPOX, $\text{C}_5\text{H}_{10}\text{O}_3$; IEPOX oxidation product, $\text{C}_4\text{H}_8\text{O}_3$; hydroxymethyl-methyl- α -lactone (HMML), $\text{C}_4\text{H}_6\text{O}_4$; MVK hydroperoxy-carbonyl (MVKPC), $\text{C}_4\text{H}_6\text{O}_3$; isoprene nitrate, $\text{C}_5\text{H}_9\text{NO}_4$). A total of 206 ions are needed to capture 99% of the downward flux. Overall, we see that the total downward VOC-C fluxes are controlled by a far larger set of species than is the case for the upward fluxes, which agrees with findings from Millet et al. (2018) over a mixed temperate forest.

In the following sections (3.2 and 3.3) we compare the aggregated VOC fluxes with those predicted by the GEOS-Chem CTM. We then examine the key environmental and chemical drivers of flux variability and of the associated model biases (3.4).

3.2 Total upward VOC-C fluxes are well-simulated by GEOS-Chem but downward fluxes are not

Figure 2 compares the total measured and modeled VOC-C fluxes. The observed net and upward VOC-C fluxes are broadly captured by the model, which exhibits a small positive bias (21-32% for the campaign as a whole) in both cases that exceeds the statistical and calibration uncertainties shown in **Fig. 2**. We see that the net observed fluxes (mean $F_{C,net,obs.} = 2.5 \times 10^{12}$ atoms C cm^{-2} s^{-1}) are controlled by and nearly equal to the upward fluxes ($F_{C,up,obs} = 2.8 \times 10^{12}$ atoms C cm^{-2} s^{-1}), revealing this to be a primarily emitting ecosystem—and this feature is also well-represented by the model ($F_{C,net,mod} = 3.3 \times 10^{12}$ atoms C cm^{-2} s^{-1} versus $F_{C,up,mod} = 3.4 \times 10^{12}$ atoms C cm^{-2} s^{-1}). Two daytime peaks are observed in the net and upward flux diel profiles (**Fig. 2d-e**): one between 08:00 and 11:00 MDT that is missing from the model, and one between 12:00 and 15:00 MDT. The morning peak is a consequence of a diurnal mountain-valley flow pattern previously documented at this site (Ortega et al., 2014) (**S6, Fig. S12**) while the afternoon peak arises from the temperature and light dependence of VOC emissions.

The GEOS-Chem model successfully represents ~50% of the day-to-day upward flux variability seen in the observations (slope = 1.3; $r^2 = 0.48$ for the daytime means). This demonstrates some fidelity at reproducing the environmental drivers of VOC-C emissions but leaves over half the day-to-day variability unresolved. The model also exhibits a systematic and sustained terpene flux underestimate from 2-7 September during intense rains (Fig. S13), and this is discussed further in Section 3.4.

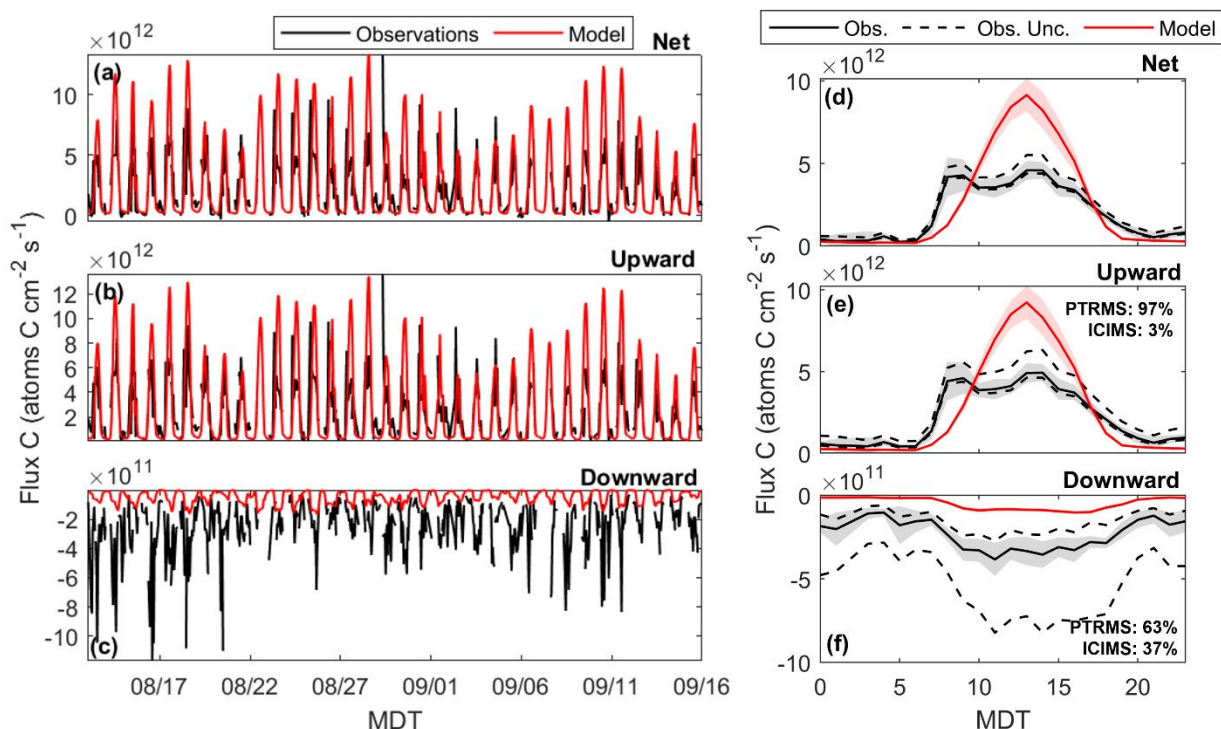


Figure 2: Summary of observed and modeled VOC-C fluxes. a-c) Observed (black) and modeled (red) net, upward, and downward VOC-carbon fluxes. d-f) Corresponding mean diel flux profiles. Shaded regions show 95% confidence intervals. Dashed lines indicate the upper and lower calibration uncertainties. Percentages of the total flux captured by the PTRMS and ICIMS are displayed inset.

The model has far less success at predicting the downward VOC-C fluxes, with a negative model bias that averages more than a factor of four (mean $F_{C,down,mod.} = -6.2 \times 10^{10}$ atoms C cm⁻² s⁻¹ versus $F_{C,down,obs.} = -2.6 \times 10^{11}$ atoms C cm⁻² s⁻¹). Calibration uncertainties (which could increase the observed total by up to 2.5× or decrease it by 1.5×) are insufficient to resolve the disparity. The model also fails to capture any of the observed day-to-day variability in the downward fluxes, with an overall model-measurement r^2 of 0.01 for the daytime means. The observed downward fluxes

are greatest during smoky and warm periods (16-19 August, 30 August – 01 September, 07-11 September) when enhanced levels of oxygenated VOCs from advected fire plumes and increased precursor emissions dry deposit to the relatively low-concentration forest canopy below. The model fares significantly worse at representing the downward VOC-C flux variability during these periods (when the two are anti-correlated) compared to the clear sky days ($r^2 = 0.22$). We return to this point in more detail later.

We can explore the causes of the large model $F_{C,down}$ bias by examining the effective deposition velocity ($v_{d,eff}$) and concentration ($[VOC-C]_{down}$) for the aggregated species undergoing downward flux ($v_{d,eff} = F_{C,down} / [VOC-C]_{down}$). **Figure 3** compares the modeled and observed diel profiles for $v_{d,eff}$ and $[VOC-C]_{down}$. The modeled and observed diel profile shapes are consistent in each case: $v_{d,eff}$ peaks with turbulent mixing during daytime whereas $[VOC-C]_{down}$ shows an afternoon decrease due to oxidative loss. However, the observations reveal sustained deposition through the night when the model predicts near-zero $v_{d,eff}$. This nighttime deposition implies that in-canopy turbulence is sufficient to drive appreciable nonstomatal loss at this time—a process that is absent from the model. Considering both day and night, the model underpredicts both $v_{d,eff}$ and $[VOC-C]_{down}$ but the latter disparity is larger (factor of 3.7 for the 24-hour average versus 1.7 for $v_{d,eff}$). While the v_d discrepancy bears further investigation, we conclude that underestimated and missing VOC-C mass is the main driver of the model downward flux bias found here.

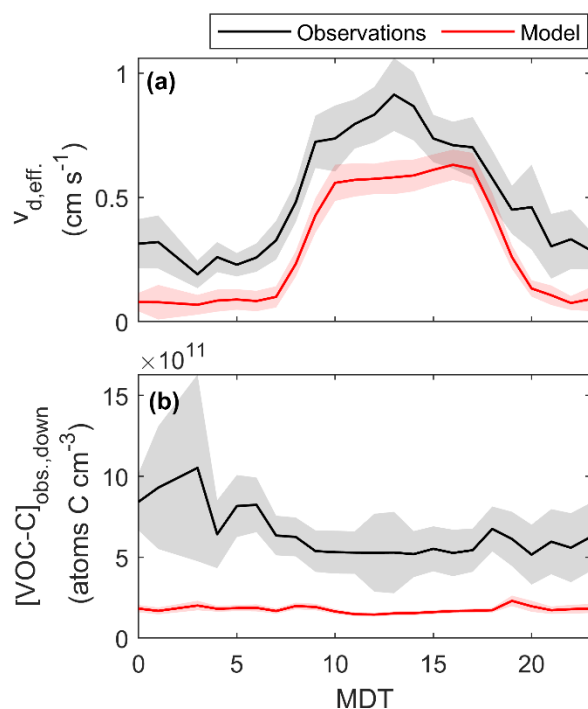


Figure 3: Mean diel profiles for the measured (black) and modeled (red) a) effective deposition velocities ($v_{d,eff}$) and b) concentrations ($[\text{VOC-C}]_{\text{down}}$) for all VOCs exhibiting downward fluxes. Shaded areas indicate 95% confidence intervals.

3.3 Total reactivity fluxes are controlled by few, known compounds

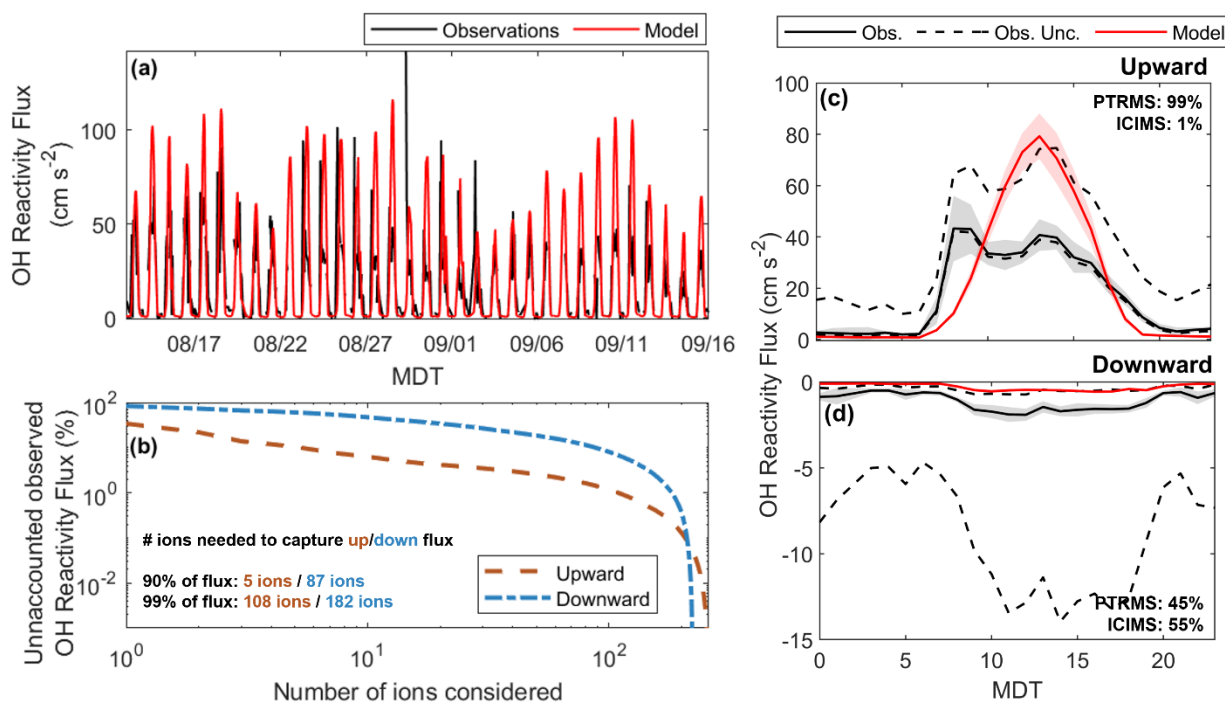


Figure 4: Summary of observed and modeled OH reactivity fluxes. a) Time series of modeled (red) and

observed (black) OH reactivity fluxes ($k_{\text{OH}+\text{VOC}} \cdot F_{\text{VOC}}$). b) Percentage of unaccounted upward (orange) and downward (blue) OH reactivity flux as a function of the number of ions considered. Mean diel c) upward and d) downward OH reactivity fluxes are also shown. Observed and modeled fluxes are displayed respectively as the solid black and red lines with 95% confidence intervals about the mean. Upper and lower uncertainty bounds associated with VOC calibration and assigned reaction rate coefficients are plotted as the black dashed lines. Percentages of the total reactivity flux captured by the PTRMS and ICIMS are indicated inset.

While the VOC-C fluxes discussed above quantify the exchange of organic mass between the forest canopy and atmosphere, the resulting impact on atmospheric chemistry can be described via the oxidant reactivity fluxes $F_{R_{Y+\text{VOC}}} = \sum k_{Y+\text{VOC}} \cdot F_{\text{VOC}}$. Here, $k_{Y+\text{VOC}}$ is the rate coefficient for reaction between a given VOC and an oxidant Y while F_{VOC} is the molar forest-atmosphere flux of that VOC. $F_{R_{Y+\text{VOC}}}$ (cm s^{-2}) is equivalent to the time derivative of reactivity ($R_{Y+\text{VOC}} = \sum k_{Y+\text{VOC}} \cdot X_{\text{VOC}}$; s^{-1}), scaled to mixing height ($F_{R_{Y+\text{VOC}}} = h \cdot \frac{dR_{Y+\text{VOC}}}{dt}$), and thus directly characterizes the influence of surface fluxes on ambient oxidant reactivity (Millet et al., 2018).

We derive OH and O_3 reactivity fluxes by applying literature rate coefficients to the corresponding measured and modeled VOC fluxes (Atkinson et al., 2006; 1990; Atkinson & Arey, 2003; Chen et al., 2015; Grosjean et al., 1993; Grosjean & Grosjean, 1999; Lee et al., 2006; Reissell et al., 2000; Richters et al., 2015; Stedman & Niki, 1973). For species with known molecular formulae but unknown structure we obtain $k_{\text{OH}+\text{VOC}}$ using the parameterization introduced by Donahue et al. (2013), and $k_{\text{O}_3+\text{VOC}}$ based on the computed double bond equivalent (DBE) as described in S7. A factor of 10 uncertainty in $k_{Y+\text{VOC}}$ is estimated for such species by applying the same methodology to all measured species with known structure and $k_{Y+\text{VOC}}$. Further details are provided in S7 (Chan et al., 2016; Helmig et al., 2007; D. Kim et al., 2011). Total $F_{R_{Y+\text{VOC}}}$ uncertainties are propagated from those in the instrumental sensitivities (as described earlier) and in the assigned k values, and are dominated by the latter. Resulting uncertainties for $F_{R_{\text{OH}}}$ can change the net, upward, and downward fluxes by up to 55%, 85%, and 8 \times , respectively. Uncertainties for $F_{R_{\text{O}_3}}$ can change the net, upward, and downward fluxes by up to 23%, 42%, and 7 \times .

Figures 4 and 5 summarize the observed and modeled OH and O₃ reactivity fluxes during the study period. In both cases we see a positive model bias of 16-30% in the net reactivity exchange (mean values: $F_{\text{ROH,net}} = 27.4 \text{ cm s}^{-2}$ versus 21.1 cm s^{-2} , $F_{\text{RO3,net}} = 5.0 \times 10^{-5} \text{ cm s}^{-2}$ versus $4.3 \times 10^{-5} \text{ cm s}^{-2}$). Only 5 ions account for over 90% of $F_{\text{ROH,up,obs}}$: 232-MBO (66%), Σ MT (12%), isoprene, Σ SQT, and acetaldehyde. Similarly, only 8 ions account for over 90% of $F_{\text{RO3,up,obs}}$ (Fig. 5b) with fluxes in this case primarily driven by Σ SQT (73%) and Σ MT (10%), followed by 232-MBO, isoprene, and butene. Many more ions are required to capture $F_{\text{ROH,down,obs.}}$ and $F_{\text{RO3,down,obs.}}$ (Fig. 5c+d; Fig. 6c+d); however, these fluxes are much smaller than the upward reactivity exchange as these more reactive compounds are primarily lost through chemistry rather than deposition. As with the carbon-based fluxes, the model has far more success at predicting day-to-day variability in the upward than in the downward reactivity exchange ($r_{\text{ROH,up}}^2 = 0.39$, $r_{\text{ROH,down}}^2 = 0.07$; $r_{\text{RO3,up}}^2 = 0.53$; $r_{\text{RO3,down}}^2 = 0.02$ for the daytime means). Collectively, these findings mirror those for the VOC-C fluxes, where: 1) $F_{\text{Ry+VOC,net}}$ is primarily controlled by few, commonly measured and modeled emitting species; 2) far more ions are required to capture the downward reactivity fluxes; and 3) the GEOS-Chem model captures the general magnitude and much of the day-to-day variability in the upward fluxes but fails at both for the downward fluxes.

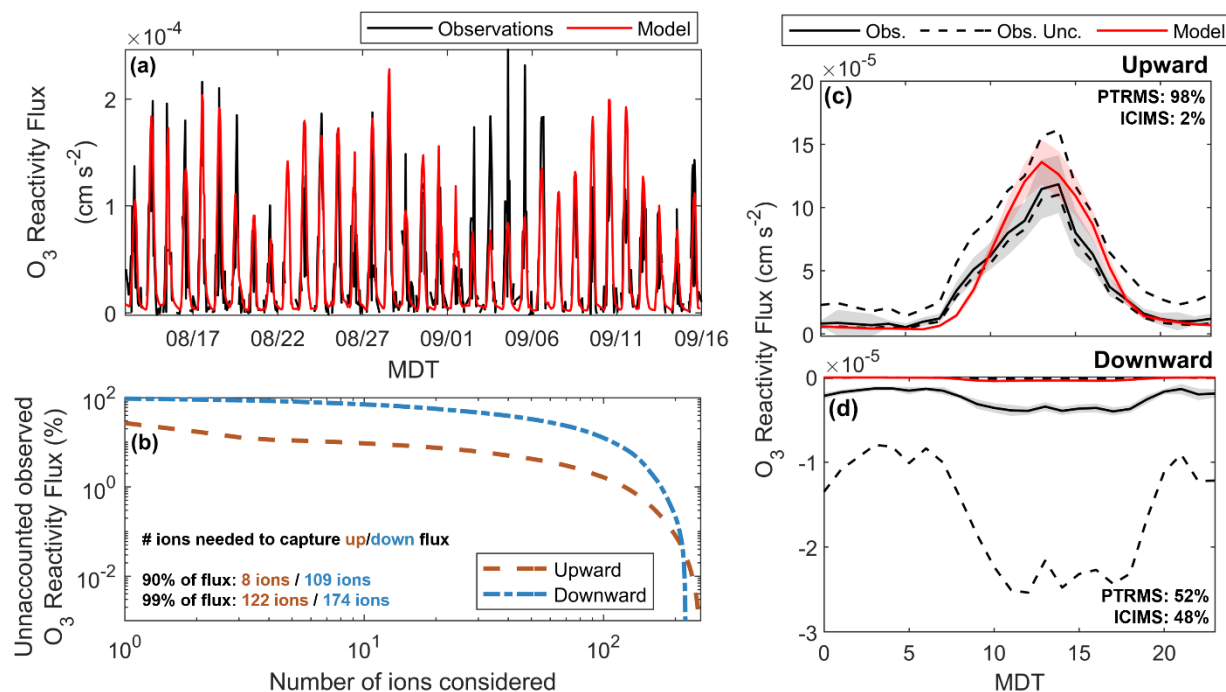


Figure 5: Summary of observed and modeled O₃ reactivity fluxes. a) Time series of modeled (red) and observed (black) O₃ reactivity fluxes ($k_{\text{O3+VOC}} \cdot F_{\text{VOC}}$). b) Percentage of unaccounted upward (orange) and downward (blue) O₃ reactivity flux as a function of the number of ions considered. Mean diel c) upward

and d) downward O₃ reactivity fluxes are also shown. Observed and modeled fluxes are displayed respectively as the solid black and red lines with 95% confidence intervals about the mean. Upper and lower uncertainty bounds associated with VOC calibration and assigned reaction rate coefficients are plotted as the black dashed lines. Percentages of the total reactivity flux captured by the PTRMS and ICIMS are indicated inset.

The above findings highlight some priorities for updating current CTMs. In particular, the standard GEOS-Chem implementation does not feature any explicit chemistry for 232-MBO and Σ SQT; their emissions are only included to compute parameterized yields of acetone and SOA. Our findings here that 232-MBO and Σ SQT respectively account for the bulk of measured OH and O₃ reactivity fluxes demonstrate that this model omission neglects key regional sources of reactivity. We recommend explicit representation of both species in CTMs to reduce such biases and for better predictions of surface-atmosphere exchange and its chemical impacts.

In the following section we discuss the environmental and chemical drivers of flux variability and model-measurement disparities identified above.

3.4 Drivers of flux variability and of model-measurement disparities

3.4.1 Model upward flux biases arise from known species; downward flux biases arise from diverse species

Figure 6 groups the observed and modeled VOC-C fluxes by carbon oxidation state (OS_c) and DBE. DBE estimates the number of double bonds or rings for a given VOC from its molecular formula as $DBE = 1 + n_c - n_H/2 + n_N/2$, and provides a first-order approximation of reactivity against OH addition or ozonolysis (Pagonis et al., 2019; Yuan et al., 2017). OS_c is computed as $OS_c = 2n_O/n_C - n_H/n_C$ and we use it here as a general marker of oxidation level and volatility (lower OS_c ~ higher volatility) (Isaacman-Vanwertz et al., 2018; Kroll et al., 2011). When there is an assumed nitrate group present ($n_N \geq 1$ and $n_O \geq 3$), OS_c is derived instead as $2n_O/n_C - n_H/n_C + 5n_N/n_C$. Based on these indices, **Figure 6** reveals significantly more chemical diversity in the observations than in the model predictions, with the model missing a large number of species with

the observed upward flux, 15 (85%) are explicitly modeled and the remaining 8 are included as lumped species. Offsetting model errors between these dominant species contribute to the aggregated model-measurement agreement seen in **Fig. 2a**. For example, predictions for 232-MBO and acetone (together 72% of the upward model VOC-C flux) are $\sim 1.6\times$ and $\sim 12\times$ too high, respectively, while those for ethanol, methanol, and isoprene are 3-4 \times too low. The latter underestimates partly reflect an understory contribution that is not accounted for by the model (**Figure S13**). As with VOC-C, model biases in the upward OH reactivity fluxes (mean $F_{\text{ROH,up}}$ bias = 5.4 cm s^{-2}) arise primarily from known and modeled species—with model overestimates for 232-MBO ($+8.0 \text{ cm s}^{-2}$) and ΣMT ($+0.2 \text{ cm s}^{-2}$) offset by underestimates for isoprene, acetaldehyde, and other species included in GEOS-Chem (-2.6 cm s^{-2}). Overall, we obtain reasonable model-observation agreement for the upward VOC-C and reactivity fluxes because the model simulates the main species that dominate these fluxes, and because of compensating errors for those species.

Fewer of the species controlling the downward VOC-C fluxes are represented in GEOS-Chem. Explicitly-modeled VOCs (e.g., $\text{C}_3\text{H}_6\text{O}_2$, HCHO, $\text{C}_2\text{H}_4\text{O}_2$) account for only 34% of the observed total, though numerous other species are included in lumped form (e.g., RCOOH, isoprene hydroxynitrates (INP), isoprene nitrates (IHN), and multiple isomers for ISOPOOH and IEPOX). Species completely missing from GEOS-Chem make up $\sim 10\%$ of the measured downward flux; these are chemically diverse, spanning $3 \leq n_{\text{C}} \leq 10$, $2 \leq n_{\text{H}} \leq 15$, and $2 \leq n_{\text{O}} \leq 6$. As with the upward fluxes, we see in the observations a greater contribution from high DBE, high OS_{c} species than is predicted by the model (**Fig. 6b, 6d**). These disparities have a greater impact on overall model performance for $F_{\text{C,down}}$ because in this case there are not a few, dominant species controlling the overall flux. However, the largest individual model biases are still due to known and modeled VOCs. Together, the explicitly modeled and lumped species (primarily $\text{C}_3\text{H}_6\text{O}_2$, HCHO, $\text{C}_5\text{H}_9\text{NO}_4$) are responsible for a downward flux bias of $-1.4 \times 10^{11} \text{ atoms C cm}^{-2} \text{ s}^{-1}$, compared to $-5.8 \times 10^{10} \text{ atoms C cm}^{-2} \text{ s}^{-1}$ for the unmodeled species. The known and modeled VOCs also make up over 85% of the total model $F_{\text{ROH,down}}$ bias (-0.92 cm s^{-2}).

3.4.2 VOC-C flux temperature and light dependence

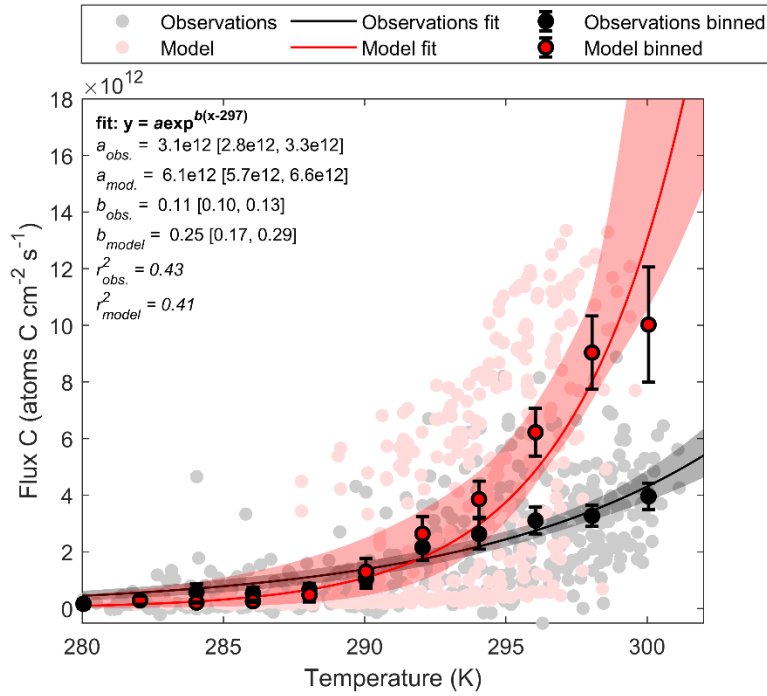


Figure 7: Environmental drivers of total net VOC-C fluxes. Observed (black) and modeled (red) VOC-C fluxes are plotted as a function of temperature. Fitted equations and parameters with associated 95% bootstrapped confidence intervals are shown inset and plotted as the black and red lines. Binned data points are indicated with the 95% confidence intervals about the mean.

We next investigate environmental drivers of the net VOC-C flux variability and model-measurement disparities. We focus in particular on surface temperature and PAR, and exclude data from 08:00-11:00 MDT to avoid the unresolved mountain-valley flow feature discussed earlier (S6). **Figure 7** plots the measured and modeled $F_{C,net}$ dependence on surface air temperature (T). Values are fit to $F_{C,net} = a \cdot \exp^{b(T-297)}$, where a is the equivalent basal emission rate and b is the effective temperature response factor (K⁻¹) for the aggregated net VOC-C fluxes (A. B. Guenther et al., 2012). The model predicts higher fitted a and b parameters than are observed, explaining the overestimated afternoon peaks in the net and upward fluxes (**Fig. 2**). We saw earlier that the majority of the observed upward fluxes were comprised of directly-emitted VOCs such as 232-MBO, Σ MT, alcohols, and isoprene, and the findings here thus suggest overestimated MEGAN v3.2 emissions factors for these species from ponderosa pine and C3 grasses.

Figure 7 shows that the modeled and observed fluxes have similar temperature dependencies for $T < 295$ K but that the model strongly overpredicts VOC-C fluxes at higher temperatures. This behavior is consistent across all modeled emitting species and for both low and high light levels (**Fig. S14**). The modeled VOC-C flux light dependence is also steeper than suggested by the observations when $T > 295$ K (**Fig. S14**). However, the two relationships are statistically indistinguishable at lower temperatures, indicating that the apparent light-dependence disparity for $T > 295$ K reflects the same temperature-dependence bias shown in **Fig 7**.

3.4.3 Rain and smoke impacts on ecosystem VOC fluxes

Rain and smoke drove large changes in the observed VOC-C and reactivity fluxes and led to the some of the largest model-measurement disparities seen during the study. **Figure 8** summarizes the observed chemical flux anomalies from these periods, which are examined in more detail next. For the following discussion we define rainy days as those with rainfall > 1 mm hr⁻¹ and smoky days as those when the observed organic aerosol (OA) mass consistently exceeded 2 $\mu\text{g m}^{-3}$; remaining days are then denoted as clear-sky periods. The OA mass was confirmed to be primarily fire-derived based on its strong correlation with the biomass burning tracers maleic anhydride (C₄H₂O₃), propanenitrile (C₃H₅N), and benzonitrile (C₇H₅N) (Coggon et al., 2019; Gilman et al., 2015) (**Fig. S16**).

Figure 8a shows that rainy periods have strong upward flux enhancements for compounds with DBE ≥ 3 and OS_c ≤ -1 . Specifically, there was an overall enhancement of 61% relative to the clear-sky periods for ΣMT , ΣSQT , monoterpene oxides (C₁₀H₁₆O, C₉H₁₄O, and C₁₀H₁₄O), and species with formulae C₁₀H₁₄, C₈H₈, and C₇H₈. Concentration gradient measurements indicate a canopy-level (ponderosa pine) source for all these compounds except ΣSQT , which are also emitted from the understory (**Fig. S15**). Previous studies have reported increased concentrations and emissions of terpenoids and other biogenic VOCs during and after rain at the branch-level (Lamb et al., 1985), above mixed and coniferous forests (Bourtsoukidis et al., 2014; Helmig et al., 1998; Holzinger et al., 2006), and at the MEFO site in particular (Kaser et al., 2013a). The latter study reported a 23 \times ΣMT flux enhancement during a hailstorm that was accompanied by enhanced

emissions of $C_{10}H_{16}O$, $C_{10}H_{14}$, $C_9H_{14}O$, $C_{10}H_{14}O$, C_8H_8 , and ΣSQT ; the authors invoked mechanical wounding of leaves as a potential cause. Wounding is an unlikely explanation for the rainfall-driven enhancements found here. On the other hand, Schade et al. (1999) documented a positive ΣMT emission dependence on humidity (after rainfall) over a ponderosa pine plantation that they attributed to increased stomatal opening and/or enhanced cuticular permeability. We speculate that such effects are also responsible for the increased VOC emissions observed in our study. Overall, the rain-induced emission enhancements for high DBE, low OS_c compounds indicate a missing source mechanism for reactive terpenoids that should be considered in models over coniferous ecosystems.

In contrast to the terpenoids, all other species exhibited decreased emissions during rainfall due to low temperatures and light levels (**Fig 8a**), leading to a 13% decrease in the aggregated VOC-C upward fluxes on rainy days relative to clear sky days. Wet conditions also allow soluble oxygenated VOCs to partition more effectively to wet surfaces, thus reducing the upward flux component for bidirectional species. The largest emission decreases ($>10^{11}$ atoms C cm⁻² s⁻¹) were observed for 232-MBO, acetone, ethanol, hydroxyacetone, and acetaldehyde. We also observe decreased downward fluxes during rainfall for many species with higher DBE across a wide OS_c range (**Fig 8b**). These include nitriles, imides, benzoic acid, phenol, and other more hydrophobic compounds that are either fire-derived or photochemically produced and have low concentrations at these times due to reduced upwind emissions.

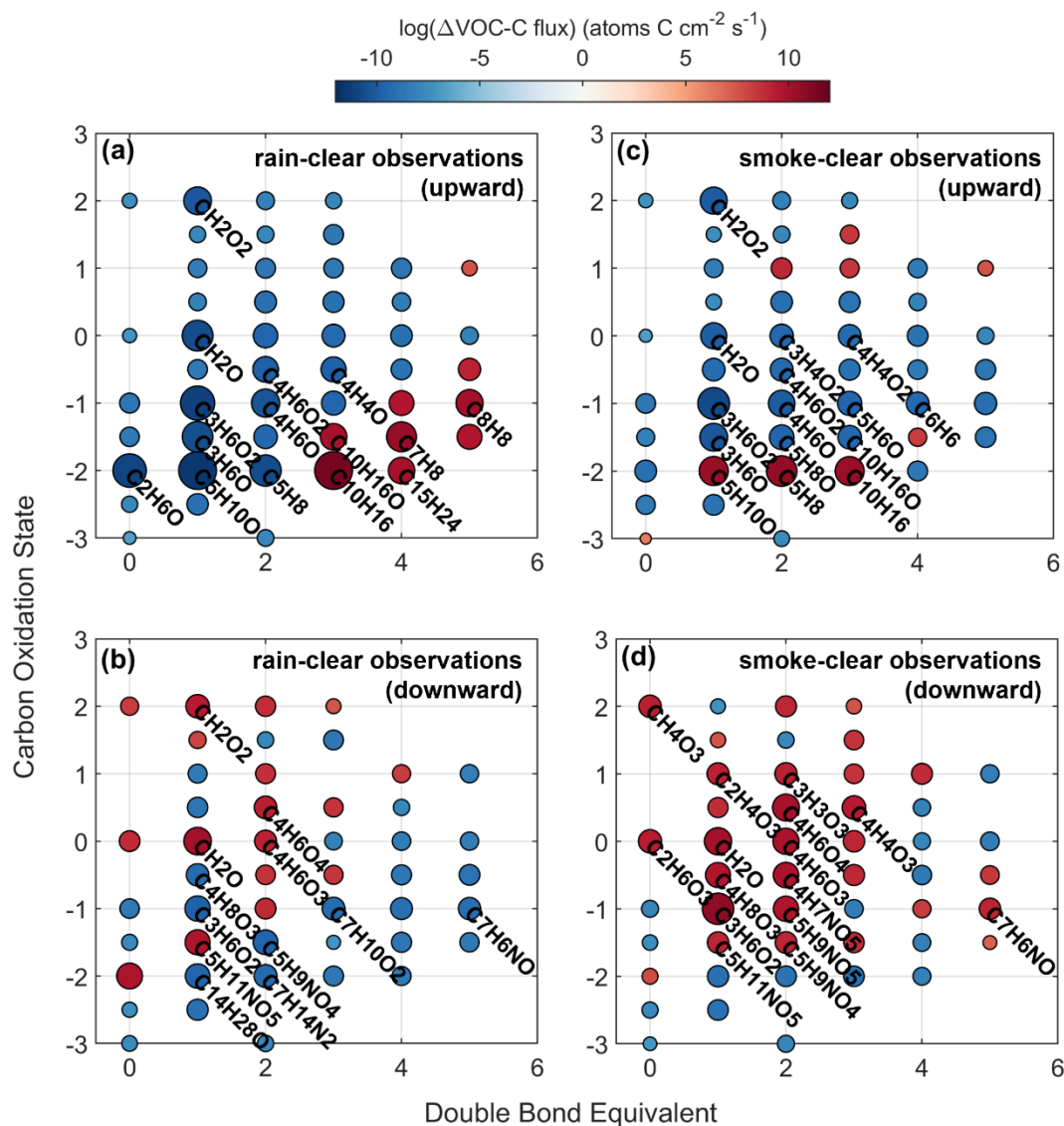


Figure 8: Effects of rain (a, b) and smoke (c, d) on observed upward and downward VOC-C fluxes. The difference in flux magnitude between rainy and clear-sky conditions and between smoky and clear-sky conditions is plotted against carbon oxidation state and double bond equivalent. Circles are colored by the log of the difference in VOC carbon flux magnitudes and sized according to the distance from $\log(\Delta\text{flux}) = 0$. Labeled on each plot are the top contributors to Δflux .

Enhanced upward fluxes of reduced compounds ($\text{OS}_c = -2$; e.g., 232-MBO, isoprene, ΣMT) are observed during smoky days (**Fig. 8c**). This enhancement is only seen for species that are primarily emitted and do not have a strong physical sink, and reflects the higher (by 1.5 °C on average) daytime temperatures on these days relative to the clear days. Meanwhile, oxygenated VOCs that

undergo bidirectional exchange, make up a large fraction of the VOC-C mass, and exhibit net emissions on clear days (e.g., acetone, hydroxyacetone, acetaldehyde, HCHO), have their upward fluxes reduced on smoky days due to higher exogenous concentrations that increase their gross deposition. The warmer temperatures on smoky days also drives a minor change in $F_{\text{ROH,up}}$ (of 0.92 cm s^{-2}), largely from isoprene (0.82 cm s^{-2}).

Downward fluxes for many other oxygenated VOCs were enhanced during smoke periods (**Fig. 8d**), in particular for species with $\text{DBE} \leq 2$ and $\text{OS}_c \geq -1$. These include acetic acid, >C2 organic acids, anhydrides, a dihydroxycarbonyl compound from IEPOX oxidation ($\text{C}_4\text{H}_8\text{O}_3$) (Bates et al., 2016), isoprene-derived organonitrates ($\text{C}_4\text{H}_7\text{NO}_5$, $\text{C}_5\text{H}_9\text{NO}_4$, $\text{C}_5\text{H}_9\text{NO}_5$) (D'ambro et al., 2017; Tsiligiannis et al., 2022), and hydroxymethyl hydroperoxide (HMHP; CH_4O_3). The >C2 organic acids observed in this study include dicarboxylic acids and ketocarboxylic acids, which are found in smoke aerosol (Kundu et al., 2010) and in SOA generated from ponderosa pine (Tomaz et al., 2018). Species identified here as succinic acid ($\text{C}_4\text{H}_6\text{O}_4$) and acetic anhydride ($\text{C}_4\text{H}_6\text{O}_3$) may also include contributions from hydroxymethyl-methyl- α -lactone (HMML) and MVK hydroperoxyl-carbonyl (MVKPC), respectively, both isoprene oxidation products. Measured isoprene emissions increased during smoke periods, which would increase the abundance of these and other oxidation products. On average, the downward oxygenated VOC-C and OH reactivity fluxes increased by 56% and 49%, respectively, on smoky days.

3.5 Instrumental ion coverage

A novel aspect of this study was the combination of high-resolution PTRMS and ICIMS mass spectra for comprehensive VOC flux characterization over an ecosystem. In this section, we describe the contributions from each instrument to this coverage.

The PTRMS detected 97% of the net upward flux compared to 3% for the ICIMS, with the latter contribution primarily from HCOOH and $\text{C}_2\text{H}_4\text{O}_2$ (**Fig. S17**). Of the 23 top species making up 90% of the upward VOC-C flux, 21 were quantified by PTRMS; the remaining two (HCOOH and

C₂H₄O₂) were quantified by both ICIMS and PTRMS. The ICIMS played more of a role for the downward fluxes, capturing 37% of the total, although the PTR-MS still covered the majority (63%). The two largest individual contributors to the downward VOC-C flux (C₃H₆O₂ and HCHO; accounting for over 30% of the total) were both detected by PTRMS. The largest downward flux contributors measured by the ICIMS (collectively accounting for 25% of the total) included oxidation products of isoprene and of 232-MBO along with >C₂ organic acids.

Meanwhile, the PTRMS captured over 98% of the total upward F_{ROH} and F_{RO_3} and therefore a vast majority of the net reactivity flux in both cases. The 5 ions accounting for nearly 90% of $F_{\text{ROH,up,obs}}$ and $F_{\text{RO}_3,\text{up,obs}}$ were all identified by PTRMS and are commonly reported using this instrument over forest ecosystems. Since the ICIMS detects more soluble oxidized products that undergo efficient deposition, it accounted for a larger share of the downward (55% of $F_{\text{ROH,down,obs}}$ and 48% of $F_{\text{RO}_3,\text{down,obs}}$) than the upward reactivity fluxes.

In general, we find that the PTRMS detected the hydrocarbons and low molecular weight oxygenated VOCs representing the bulk of the total observed VOC mass and reactivity fluxes. PTRMS measurements can therefore be used alone to provide near-complete coverage of net VOC-C fluxes and their impacts on atmospheric reactivity over this and similar ecosystems. However, ICIMS-detected species made up a significant fraction of the downward VOC fluxes, and therefore provide key information for constraining this major sink of atmospheric reactive carbon. The ICIMS also captured a wide suite of VOC oxidation products for diagnosing the chemical fate of emitted species.

While the combination of PTRMS and ICIMS provides comprehensive observational coverage for VOCs controlling atmospheric reactive carbon abundance and reactivity, the sampling configuration used here would not capture some compounds with very high volatility (e.g., low molecular weight hydrocarbons) or very low volatility (e.g., highly oxygenated organic molecules, HOM). A previous study at this site used relaxed eddy accumulation sampling with gas chromatography-flame ionization detection to quantify summertime emissions of ethene, propene,

butene and isoprene (Rhew et al., 2017). Ethene and propene fluxes together averaged $\sim 2 \times 10^{11}$ atoms C cm⁻² s⁻¹, over an order of magnitude lower than the upward VOC-C fluxes observed in this study, and their associated reactivity fluxes would likewise be small ($F_{\text{ROH}} \sim 0.7$ cm s⁻² and $F_{\text{RO3}} \sim 4 \times 10^{-7}$ cm s⁻²). In the case of lower-volatility compounds, Hunter et al. (2017) found that semivolatile and intermediate-volatility organic species not detected by PTRMS or ICIMS accounted for $\sim 10\%$ of the total observed organic carbon concentration at MEFO. Future studies employing atmospheric pressure interface time-of-flight mass spectrometry (Riva et al., 2018) or analogous techniques could help to elucidate the contributions of such species to forest-atmosphere VOC-C exchange.

4. Conclusions

Detailed measurements are needed to understand the two-way flux of VOCs between ecosystems and the atmosphere, the resulting effects on air quality, and how well that exchange is represented in models. This study provided the most comprehensive look yet at terrestrial VOC fluxes by employing two high-resolution mass spectrometers (PTRMS and ICIMS, deployed over a temperate coniferous forest) to calculate EC fluxes across the entire mass spectrum for both instruments. Of the 1261 total ions identified as VOCs, 315 exhibited detectable fluxes; 23 and 125 of these ions were required to capture 90% of the total upward and downward VOC-carbon fluxes, respectively.

Net VOC-C exchange was dominated by the upward fluxes at this site, with PTRMS-detected species accounting for 97% of the total upward flux and 63% of the total downward flux. Comparing the observations to predictions from the GEOS-Chem CTM, we find that the model was able to capture the magnitude and much of the temporal variability in the aggregated net and upward VOC-C fluxes with only modest biases. However, the model underestimated the downward VOC-C fluxes by over a factor of four, primarily due to large concentration underestimates for many relevant oxygenated VOCs. Many of these species were detected by ICIMS, highlighting the need such measurements to fully characterize VOC deposition and fate.

Along with the VOC mass fluxes, OH and O₃ reactivity fluxes were quantified to diagnose the impacts of the measured exchange on atmospheric chemistry. The net OH and O₃ reactivity fluxes (like the mass fluxes) were primarily carried by a small number of emitted species that were detected by the PTRMS and explicitly represented in the GEOS-Chem mechanism. A total of 5 and 108 ions were required to capture 90% of the upward and downward OH reactivity fluxes, respectively, fewer than in the case of the VOC-C fluxes. 232-MBO accounted for ~70% of the OH reactivity flux and should be included in CTMs. Model biases in the simulated OH reactivity fluxes primarily arose from a 232-MBO underestimate and from a missing isoprene source from the forest floor. O₃ reactivity fluxes were dominated by Σ SQT and Σ MT and were overwhelmingly (>98%) composed of PTRMS-measured species. We recommend explicit representation of Σ SQT in CTM mechanisms to correctly represent near-surface O₃ loss.

The GEOS-Chem model was generally successful in simulating the canopy-scale dependence of VOC fluxes on temperature and sunlight for $T < 295$ K, but strongly overpredicted the flux-temperature sensitivity under hotter conditions. It also failed to capture the enhanced terpenoid emissions that occurred on rainy days. Overall, the main model-measurement disparities identified here were driven by biases for species that are already accounted-for in CTMs rather than by missing species. Better model performance was achieved for the net and upward VOC-C and reactivity fluxes than for the downward fluxes. This is partly because the upward fluxes were dominated by a few major species (all of which have explicit CTM representation), and partly because of offsetting model errors between those major species.

This work has provided a chemically detailed analysis of VOC surface-atmosphere exchange for one pine forest ecosystem, and builds upon a small number of similar studies that relied solely upon PTRMS (Loubet et al., 2022; Millet et al., 2018; Park et al., 2013). Further measurements employing multiple high-resolution mass spectrometers in different ecosystems are required to better understand surface-atmosphere VOC fluxes across the full suite of relevant compounds, diagnose the underlying environmental drivers, and advance the ability of current CTMs to capture the ensuing impact on atmospheric chemistry.

Acknowledgements

This work was supported by NSF AGS 1932771 and 1932849. Measurement capabilities at UMN were also enhanced by support from the Alfred P. Sloan Foundation. The tower used in this project is maintained by NCAR and supported by the USFS. We thank Steven Alton and Paula Fornwalt of USFS for their support with site and logistics. We also thank Glenn M. Wolfe for publicly providing the MATLAB-based FluxToolbox of analysis scripts, portions of which were altered for use in this analysis. Computing resources were provided by the Minnesota Supercomputing Institute (<http://www.msi.umn.edu>) at the University of Minnesota. We acknowledge that this project occurred on the traditional territory of the Ute and Cheyenne peoples.

Data Availability Statement

Observed and simulated total VOC-C and reactivity fluxes (net, upward, and downward) and associated meteorological observations can be accessed at <https://atmoschem.umn.edu/data>. This data will be permanently archived with a DOI at <https://conservancy.umn.edu/> at the time of publication. GEOS-Chem model code is publicly available at <http://www.geos-chem.org>. The FluxToolBox code is archived at <https://github.com/AirChem>.

References

- Arneth, A., Schurgers, G., Lathiere, J., Duhl, T., Beerling, D. J., Hewitt, C. N., et al. (2011). Global terrestrial isoprene emission models: Sensitivity to variability in climate and vegetation. *Atmospheric Chemistry and Physics*, 11(15), 8037–8052. <https://doi.org/10.5194/ACP-11-8037-2011>
- Atkinson, R., Baulch, D. L., Cox, R. A., Crowley, J. N., Hampson, R. F., Hynes, R. G., et al. (2006). Atmospheric Chemistry and Physics Evaluated kinetic and photochemical data for atmospheric chemistry: Volume II-gas phase reactions of organic species The IUPAC Subcommittee on Gas Kinetic Data Evaluation for Atmospheric Chemistry. *Atmos. Chem. Phys.*, 6, 3625–4055. Retrieved from www.atmos-chem-phys.net/6/3625/2006/
- Atkinson, R. & Arey, J. (2003). Atmospheric Degradation of Volatile Organic Compounds. *Chemical Reviews*, 103(12), 4605–4638. <https://doi.org/10.1021/CR0206420/ASSET/IMAGES/MEDIUM/CR0206420E00019.GIF>
- Atkinson, R., Aschmann, S. M., & Arey, J. (1990). Rate constants for the gas-phase reactions of OH and NO₃ radicals and O₃ with sabinene and camphene at 296±2 K. *Atmospheric Environment Part A, General Topics*, 24(10), 2647–2654. [https://doi.org/10.1016/0960-1686\(90\)90144-C](https://doi.org/10.1016/0960-1686(90)90144-C)

786 Bates, K. H., & Jacob, D. J. (2019). A new model mechanism for atmospheric oxidation of isoprene: Global effects
787 on oxidants, nitrogen oxides, organic products, and secondary organic aerosol. *Atmospheric Chemistry and*
788 *Physics*, 19(14), 9613–9640. <https://doi.org/10.5194/ACP-19-9613-2019>

789 Bates, K. H., Nguyen, T. B., Teng, A. P., Crounse, J. D., Kjaergaard, H. G., Stoltz, B. M., et al. (2016). Production
790 and Fate of C4 Dihydroxycarbonyl Compounds from Isoprene Oxidation. *Journal of Physical Chemistry A*,
791 120(1), 106–117. [https://doi.org/10.1021/ACS.JPCA.5B10335/ASSET/IMAGES/LARGE/JP-2015-](https://doi.org/10.1021/ACS.JPCA.5B10335/ASSET/IMAGES/LARGE/JP-2015-10335X_0009.JPEG)
792 10335X_0009.JPEG

793 Bates, K. H., Jacob, D. J., Wang, S., Hornbrook, R. S., Apel, E. C., Kim, M. J., et al. (2021). The Global Budget of
794 Atmospheric Methanol: New Constraints on Secondary, Oceanic, and Terrestrial Sources. *Journal of*
795 *Geophysical Research: Atmospheres*, 126(4), e2020JD033439. <https://doi.org/10.1029/2020JD033439>

796 Beaver, M. R., St. Clair, J. M., Paulot, F., Spencer, K. M., Crounse, J. D., Lafranchi, B. W., et al. (2012). Importance
797 of biogenic precursors to the budget of organic nitrates: Observations of multifunctional organic nitrates by
798 CIMS and TD-LIF during BEARPEX 2009. *Atmospheric Chemistry and Physics*, 12(13), 5773–5785.
799 <https://doi.org/10.5194/ACP-12-5773-2012>

800 Berkelhammer, M., Noone, D. C., Wong, T. E., Burns, S. P., Knowles, J. F., Kaushik, A., et al. (2016). Convergent
801 approaches to determine an ecosystem's transpiration fraction. *Global Biogeochemical Cycles*, 30(6), 933–
802 951. <https://doi.org/10.1002/2016GB005392>

803 Bertram, T. H., Kimmel, J. R., Crisp, T. a., Ryder, O. S., Yatavelli, R. L. N., Thornton, J. a., et al. (2011). A field-
804 deployable, chemical ionization time-of-flight mass spectrometer. *Atmospheric Measurement Techniques*,
805 4(7), 1471–1479. <https://doi.org/10.5194/amt-4-1471-2011>

806 Bessagnet, B., Seigneur, C., & Menut, L. (2010). Impact of dry deposition of semi-volatile organic compounds on
807 secondary organic aerosols. *Atmospheric Environment*, 44, 1781–1787.
808 <https://doi.org/10.1016/j.atmosenv.2010.01.027>

809 Bi, C., Krechmer, J. E., Frazier, G. O., Xu, W., Lambe, A. T., Claflin, M. S., et al. (2021). Quantification of isomer-
810 resolved iodide chemical ionization mass spectrometry sensitivity and uncertainty using a voltage-scanning
811 approach. *Atmospheric Measurement Techniques*, 14(10), 6835–6850. [https://doi.org/10.5194/AMT-14-6835-](https://doi.org/10.5194/AMT-14-6835-2021)
812 2021

813 Boucher, O., Randall, D., Artaxo, P., Bretherton, C., Feingold, G., Forster, P., et al. (2013). Climate change 2013:
814 the physical science basis. Contribution of Working Group I to the Fifth Assessment Report of the
815 Intergovernmental Panel on Climate Change. K., Tignor, M., Allen, SK, Boschung, J., Nauels, A., Xia, Y., Bex,
816 V., and Midgley, PM, Cambridge University Press, Cambridge, UK.

817 Bourtsoukidis, E., Williams, J., Kesselmeier, J., Jacobi, S., & Bonn, B. (2014). From emissions to ambient mixing
818 ratios: Online seasonal field measurements of volatile organic compounds over a Norway spruce-dominated
819 forest in central Germany. *Atmospheric Chemistry and Physics*, 14(13), 6495–6510.
820 <https://doi.org/10.5194/acp-14-6495-2014>

821 Brophy, P., & Farmer, D. K. (2015). A switchable reagent ion high resolution time-of-flight chemical ionization
822 mass spectrometer for real-time measurement of gas phase oxidized species: Characterization from the 2013
823 southern oxidant and aerosol study. *Atmospheric Measurement Techniques*, 8(7), 2945–2959.
824 <https://doi.org/10.5194/AMT-8-2945-2015>

825 Byrne, K. A., Kiely, G., & Leahy, P. (2005). CO₂ fluxes in adjacent new and permanent temperate grasslands.
826 *Agricultural and Forest Meteorology*, 135(1–4), 82–92. <https://doi.org/10.1016/J.AGRFORMET.2005.10.005>

827 Canagaratna, M. R., Jimenez, J. L., Kroll, J. H., Chen, Q., Kessler, S. H., Massoli, P., et al. (2015). Elemental ratio
828 measurements of organic compounds using aerosol mass spectrometry: Characterization, improved
829 calibration, and implications. *Atmospheric Chemistry and Physics*, 15(1), 253–272.
830 <https://doi.org/10.5194/ACP-15-253-2015>

831 Chan, A. W. H., Kreisberg, N. M., Hohaus, T., Campuzano-Jost, P., Zhao, Y., Day, D. A., et al. (2016). Speciated
832 measurements of semivolatile and intermediate volatility organic compounds (S/IVOCs) in a pine forest

during BEACHON-RoMBAS 2011. *Atmos. Chem. Phys.*, *16*, 1187–1205. <https://doi.org/10.5194/acp-16-1187-2016>

Chen, H., Ren, Y., Cazaunau, M., Daële, V., Hu, Y., Chen, J., & Mellouki, A. (2015). Rate coefficients for the reaction of ozone with 2-and 3-carene. *Chemical Physics Letters*, *621*, 71–77. <https://doi.org/10.1016/j.cplett.2014.12.056>

Chen, X., Millet, D. B., Singh, H. B., Wisthaler, A., Apel, E. C., Atlas, E. L., et al. (2019). On the sources and sinks of atmospheric VOCs: an integrated analysis of recent aircraft campaigns over North America. *Atmospheric Chemistry and Physics*, *19*(14), 9097–9123. <https://doi.org/10.5194/ACP-19-9097-2019>

Coggon, M. M., Lim, C. Y., Koss, A. R., Sekimoto, K., Yuan, B., Gilman, J. B., et al. (2019). OH chemistry of non-methane organic gases (NMOGs) emitted from laboratory and ambient biomass burning smoke: Evaluating the influence of furans and oxygenated aromatics on ozone and secondary NMOG formation. *Atmospheric Chemistry and Physics*, *19*(23), 14875–14899. <https://doi.org/10.5194/ACP-19-14875-2019>

D’ambro, E. L., Lee, B. H., Liu, J., Shilling, J. E., Gaston, C. J., Lopez-Hilfiker, F. D., et al. (2017). Molecular composition and volatility of isoprene photochemical oxidation secondary organic aerosol under low-and high-NO_x conditions. *Atmos. Chem. Phys.*, *17*, 159–174. <https://doi.org/10.5194/acp-17-159-2017>

DeCarlo, P. F., Kimmel, J. R., Trimborn, A., Northway, M. J., Jayne, J. T., Aiken, A. C., et al. (2006). Field-deployable, high-resolution, time-of-flight aerosol mass spectrometer. *Analytical Chemistry*, *78*(24), 8281–8289. https://doi.org/10.1021/AC061249N/SUPPL_FILE/AC061249NSI20060905_075156.PDF

Donahue, N. M., Chuang, W., Epstein, S. A., Kroll, J. H., Worsnop, D. R., Robinson, A. L., et al. (2013). Why do organic aerosols exist? Understanding aerosol lifetimes using the two-dimensional volatility basis set. *Environmental Chemistry*, *10*(3), 151–157. <https://doi.org/10.1071/EN13022>

Fantechi, G., Jensen, N. R., Hjorth, J., & Peeters, J. (1998). Mechanistic studies of the atmospheric oxidation of methyl butenol by OH radicals, ozone and NO₃ radicals. *Atmospheric Environment*, *32*(20), 3547–3556. [https://doi.org/10.1016/S1352-2310\(98\)00061-2](https://doi.org/10.1016/S1352-2310(98)00061-2)

Ferronato, C., Orlando, J. J., & Tyndall, G. S. (1998). Rate and mechanism of the reactions of OH and Cl with 2-methyl-3-buten-2-ol. *Journal of Geophysical Research: Atmospheres*, *103*(D19), 25579–25586. <https://doi.org/10.1029/98JD00528>

Fischer, L., Breitenlechner, M., Canaval, E., Scholz, W., Striednig, M., Graus, M., et al. (2021). First eddy covariance flux measurements of semi-volatile organic compounds with the PTR3-TOF-MS. *Atmospheric Measurement Techniques*, *14*(12), 8019–8039. <https://doi.org/10.5194/AMT-14-8019-2021>

Fisher, J. A., Atlas, E. L., Barletta, B., Meinardi, S., Blake, D. R., Thompson, C. R., et al. (2018). Methyl, Ethyl, and Propyl Nitrates: Global Distribution and Impacts on Reactive Nitrogen in Remote Marine Environments. *Journal of Geophysical Research: Atmospheres*, *123*(21), 12,429–12,451. <https://doi.org/10.1029/2018JD029046>

Foken, T., & Wichura, B. (1996). Tools for quality assessment of surface-based flux measurements. *Agricultural and Forest Meteorology*, *78*(1–2), 83–105. [https://doi.org/10.1016/0168-1923\(95\)02248-1](https://doi.org/10.1016/0168-1923(95)02248-1)

Fulgham, S. R., Brophy, P., Link, M., Ortega, J., Pollack, I., & Farmer, D. K. (2019). Seasonal Flux Measurements over a Colorado Pine Forest Demonstrate a Persistent Source of Organic Acids. *ACS Earth and Space Chemistry*, *3*(9), 2017–2032. research-article. <https://doi.org/10.1021/acsearthspacechem.9b00182>

Giglio, L., Randerson, J. T., & Van Der Werf, G. R. (2013). Analysis of daily, monthly, and annual burned area using the fourth-generation global fire emissions database (GFED4). *Journal of Geophysical Research: Biogeosciences*, *118*(1), 317–328. <https://doi.org/10.1002/JGRG.20042>

Gilman, J. B., Lerner, B. M., Kuster, W. C., Goldan, P. D., Warneke, C., Veres, P. R., et al. (2015). Biomass burning emissions and potential air quality impacts of volatile organic compounds and other trace gases from fuels common in the US. *Atmospheric Chemistry and Physics*, *15*(24), 13915–13938. <https://doi.org/10.5194/ACP-15-13915-2015>

- 879 Glasius, M., & Goldstein, A. H. (2016). Recent Discoveries and Future Challenges in Atmospheric Organic
880 Chemistry. *Environmental Science and Technology*, 50(6), 2754–2764.
881 https://doi.org/10.1021/ACS.EST.5B05105/ASSET/IMAGES/LARGE/ES-2015-051053_0003.JPEG
- 882 Goldstein, A. H., & Galbally, I. E. (2007). Known and unexplored organic constituents in the earth's atmosphere.
883 *Environmental Science and Technology*, 41(5), 1514–1521. <https://doi.org/10.1021/es072476p>
- 884 Grosjean, D., Grosjean, E., & Williams, E. L. (1993). Rate constants for the gas-phase reactions of ozone with
885 unsaturated alcohols, esters, and carbonyls. *International Journal of Chemical Kinetics*, 25(9), 783–794.
886 <https://doi.org/10.1002/KIN.550250909>
- 887 Grosjean, E., & Grosjean, D. (1999). Rate Constants for the Gas-Phase Reaction of Ozone with Unsaturated
888 Oxygenates. *International Journal of Chemical Kinetics*, 30, 21–29. [https://doi.org/10.1002/\(SICI\)1097-](https://doi.org/10.1002/(SICI)1097-4601(1998)30:1)
889 [4601\(1998\)30:1](https://doi.org/10.1002/(SICI)1097-4601(1998)30:1)
- 890 Guenther, A., Karl, T., Harley, P., Wiedinmyer, C., Palmer, P. I., & Geron, C. (2006). Estimates of global terrestrial
891 isoprene emissions using MEGAN (Model of Emissions of Gases and Aerosols from Nature). *Atmospheric*
892 *Chemistry and Physics*, 6(11), 3181–3210. <https://doi.org/10.5194/acp-6-3181-2006>
- 893 Guenther, A., Jiang, X., Heald, C. L., Sakulyanontvittaya, T., Duhl, T., Emmons, L. K., & Wang, X. (2012). The
894 model of emissions of gases and aerosols from nature version 2.1 (MEGAN2.1): An extended and updated
895 framework for modeling biogenic emissions. *Geoscientific Model Development*, 5(6), 1471–1492.
896 <https://doi.org/10.5194/gmd-5-1471-2012>
- 897 Guenther, A., Jiang, X., Shah, T., Huang, L., Kemball-Cook, S., & Yarwood, G. (2020). Model of Emissions of
898 Gases and Aerosol from Nature Version 3 (MEGAN3) for Estimating Biogenic Emissions BT - Air Pollution
899 Modeling and its Application XXVI. In C. Mensink, W. Gong, & A. Hakami (Eds.) (pp. 187–192). Cham:
900 Springer International Publishing.
- 901 Heikes, B. G. (2002). Atmospheric methanol budget and ocean implication. *Global Biogeochemical Cycles*, 16(4),
902 1–13. <https://doi.org/10.1029/2002GB001895>
- 903 Helmig, D., Greenberg, J., Guenther, A., Zimmerman, P., & Geron, C. (1998). Volatile organic compounds and
904 isoprene oxidation products at a temperate deciduous forest site. *Journal of Geophysical Research:*
905 *Atmospheres*, 103(D17), 22397–22414. <https://doi.org/10.1029/98JD00969>
- 906 Helmig, D., Ortega, J., Duhl, T., Tanner, D., Guenther, A., Harley, P., et al. (2007). Sesquiterpene emissions from
907 pine trees - Identifications, emission rates and flux estimates for the contiguous United States. *Environmental*
908 *Science and Technology*, 41(5), 1545–1553. <https://doi.org/10.1021/es0618907>
- 909 Hoesly, R. M., Smith, S. J., Feng, L., Klimont, Z., Janssens-Maenhout, G., Pitkanen, T., et al. (2018). Historical
910 (1750–2014) anthropogenic emissions of reactive gases and aerosols from the Community Emissions Data
911 System (CEDS). *Geoscientific Model Development*, 11(1), 369–408. [https://doi.org/10.5194/GMD-11-369-](https://doi.org/10.5194/GMD-11-369-2018)
912 [2018](https://doi.org/10.5194/GMD-11-369-2018)
- 913 Holzinger, R. (2015). PTRwid: A new widget tool for processing PTR-TOF-MS data. *Atmospheric Measurement*
914 *Techniques*, 8(9), 3903–3922. <https://doi.org/10.5194/AMT-8-3903-2015>
- 915 Holzinger, R., Lee, A., McKay, M., & Goldstein, A. H. (2006). *Atmospheric Chemistry and Physics Seasonal*
916 *variability of monoterpene emission factors for a Ponderosa pine plantation in California*. *Atmos. Chem. Phys*
917 (Vol. 6). Retrieved from www.atmos-chem-phys.net/6/1267/2006/
- 918 Hu, L., Millet, D. B., Baasandorj, M., Griffis, T. J., Turner, P., Helmig, D., et al. (2015). Isoprene emissions and
919 impacts over an ecological transition region in the U.S. Upper Midwest inferred from tall tower
920 measurements. *Journal of Geophysical Research: Atmospheres*, 120(8), 3553–3571.
921 <https://doi.org/10.1002/2014JD022732>
- 922 Huang, G., Brook, R., Crippa, M., Janssens-Maenhout, G., Schieberle, C., Dore, C., et al. (2017). Speciation of
923 anthropogenic emissions of non-methane volatile organic compounds: a global gridded data set for 1970–2012.
924 *Atmospheric Chemistry and Physics Discussions*, 1–36. <https://doi.org/10.5194/acp-2017-65>

925 Hunter, J. F., Day, D. A., Palm, B. B., Yatavelli, R. L. N., Chan, A. W. H., Kaser, L., et al. (2017). Comprehensive
 926 characterization of atmospheric organic carbon at a forested site. *Nature Geoscience* 2017 10:10, 10(10), 748–
 927 753. <https://doi.org/10.1038/ngeo3018>

928 Isaacman-Vanwertz, G., Massoli, P., O'Brien, R., Lim, C., Franklin, J. P., Moss, J. A., et al. (2018). Chemical
 929 evolution of atmospheric organic carbon over multiple generations of oxidation. *Nature Chemistry* 2018 10:4,
 930 10(4), 462–468. <https://doi.org/10.1038/s41557-018-0002-2>

931 Iyer, S., Lopez-Hilfiker, F., Lee, B. H., Thornton, J. A., & Kurtén, T. (2016). Modeling the Detection of Organic and
 932 Inorganic Compounds Using Iodide-Based Chemical Ionization.

933 Jacob, D. J., Field, B. D., Jin, E. M., Bey, I., Li, Q., Logan, J. A., et al. (2002). Atmospheric budget of acetone.
 934 *Journal of Geophysical Research: Atmospheres*, 107(9–10). <https://doi.org/10.1029/2001jd000694>

935 Karl, T., Hansel, a., Cappellin, L., Kaser, L., Herdinger-Blatt, I., & Jud, W. (2012). Selective measurements of
 936 isoprene and 2-methyl-3-buten-2-ol based on NO⁺ ionization mass spectrometry. *Atmospheric Chemistry and*
 937 *Physics*, 12(24), 11877–11884. <https://doi.org/10.5194/acp-12-11877-2012>

938 Karl, T., Kaser, L., & Turnipseed, A. (2014). Eddy covariance measurements of isoprene and 232-MBO based on
 939 NO + time-of-flight mass spectrometry. *International Journal of Mass Spectrometry*, 365–366, 15–19.
 940 <https://doi.org/10.1016/j.ijms.2013.12.002>

941 Kaser, L., Karl, T., Guenther, A., Graus, M., Schnitzhofer, R., Turnipseed, A., et al. (2013a). Undisturbed and
 942 disturbed above canopy ponderosa pine emissions: PTR-TOF-MS measurements and MEGAN 2.1 model
 943 results. *Atmospheric Chemistry and Physics*, 13(23), 11935–11947. [https://doi.org/10.5194/acp-13-11935-](https://doi.org/10.5194/acp-13-11935-2013)
 944 2013

945 Kaser, L., Karl, T., Schnitzhofer, R., Graus, M., Herdinger-Blatt, I. S., DiGangi, J. P., et al. (2013b). Comparison of
 946 different real time VOC measurement techniques in a ponderosa pine forest. *Atmospheric Chemistry and*
 947 *Physics*, 13(5), 2893–2906. <https://doi.org/10.5194/acp-13-2893-2013>

948 Kim, D., Stevens, P. S., & Hites, R. A. (2011). Rate constants for the gas-phase reactions of OH and O₃ with β-
 949 ocimene, β-myrcene, and α-and β-farnesene as a function of temperature. *Journal of Physical Chemistry A*,
 950 115(4), 500–506. <https://doi.org/10.1021/jp111173s>

951 Kim, S., Karl, T., Guenther, A., Tyndall, G., Orlando, J., Harley, P., et al. (2010). Emissions and ambient
 952 distributions of Biogenic Volatile Organic Compounds (BVOC) in a ponderosa pine ecosystem: Interpretation
 953 of PTR-MS mass spectra. *Atmospheric Chemistry and Physics*, 10(4), 1759–1771. [https://doi.org/10.5194/acp-](https://doi.org/10.5194/acp-10-1759-2010)
 954 10-1759-2010

955 Kroll, J. H., Donahue, N. M., Jimenez, J. L., Kessler, S. H., Canagaratna, M. R., Wilson, K. R., et al. (2011). Carbon
 956 oxidation state as a metric for describing the chemistry of atmospheric organic aerosol. *Nat. Chem.*, 3(2), 133.
 957 <https://doi.org/10.1038/nchem.948>

958 Kundu, S., Kawamura, K., Andreae, T. W., Hoffer, A., & Andreae, M. O. (2010). Molecular distributions of
 959 dicarboxylic acids, ketocarboxylic acids and α-dicarbonyls in biomass burning aerosols: Implications for
 960 photochemical production and degradation in smoke layers. *Atmospheric Chemistry and Physics*, 10(5), 2209–
 961 2225. <https://doi.org/10.5194/ACP-10-2209-2010>

962 Lamb, B., Westberg, H., Allwine, G., & Quarles, T. (1985). Biogenic hydrocarbon emissions from deciduous and
 963 coniferous trees in the United States. *Journal of Geophysical Research*, 90, 2380–2390.
 964 <https://doi.org/10.1029/JD090iD01p02380>

965 Lary, D. J., & Shallcross, D. E. (2000). Central role of carbonyl compounds in atmospheric chemistry. *Journal of*
 966 *Geophysical Research Atmospheres*, 105(D15), 19771–19778. <https://doi.org/10.1029/1999JD901184>

967 Lee, A., Goldstein, A. H., Keywood, M. D., Gao, S., Varutbangkul, V., Bahreini, R., et al. (2006). Gas-phase
 968 products and secondary aerosol yields from the ozonolysis of ten different terpenes. *Journal of Geophysical*
 969 *Research Atmospheres*, 111(7), 1–18. <https://doi.org/10.1029/2005JD006437>

970 Lee, B. H., Lopez-hilfiker, F. D., Mohr, C., Kurten, T., Worsnop, D. R., & Joel, A. (2014). An Iodide-Adduct High-
 971 Resolution Time-of-Flight Chemical- Ionization Mass Spectrometer: Application to Atmospheric Inorganic
 972 and Organic Compounds. *Environ.Sci. Technol.*, 48, 6309–6317. <https://doi.org/10.1021/es500362a>

973 Lee, X., Massman, W. J., & Law, B. (2005). Handbook of Micrometeorology. *Handbook of Micrometeorology*, 29,
 974 250. Retrieved from
 975 https://books.google.com/books/about/Handbook_of_Micrometeorology.html?id=IJ_19RkTfBQC

976 Lin, H., Jacob, D. J., Lundgren, E. W., Sulprizio, M. P., Keller, C. A., Fritz, T. M., et al. (2021). Harmonized
 977 Emissions Component (HEMCO) 3.0 as a versatile emissions component for atmospheric models: Application
 978 in the GEOS-Chem, NASA GEOS, WRF-GC, CESM2, NOAA GEFS-Aerosol, and NOAA UFS models.
 979 *Geoscientific Model Development*, 14(9), 5487–5506. <https://doi.org/10.5194/GMD-14-5487-2021>

980 Link, M. F., Brophy, P., Fulgham, S. R., Murschell, T., & Farmer, D. K. (2021). Isoprene versus Monoterpenes as
 981 Gas-Phase Organic Acid Precursors in the Atmosphere. *ACS Earth and Space Chemistry*, 5(6), 1600–1612.
 982 [https://doi.org/10.1021/ACSEARTHSPACECHEM.1C00093/ASSET/IMAGES/LARGE/SP1C00093_0010.J](https://doi.org/10.1021/ACSEARTHSPACECHEM.1C00093/ASSET/IMAGES/LARGE/SP1C00093_0010.JPEG)
 983 PEG

984 Lopez-Hilfiker, F. D., Mohr, C., Ehn, M., Rubach, F., Kleist, E., Wildt, J., et al. (2014). A novel method for online
 985 analysis of gas and particle composition: Description and evaluation of a filter inlet for gases and AEROSols
 986 (FIGAERO). *Atmospheric Measurement Techniques*, 7(4), 983–1001. [https://doi.org/10.5194/AMT-7-983-](https://doi.org/10.5194/AMT-7-983-2014)
 987 2014

988 Lopez-Hilfiker, F. D., Iyer, S., Mohr, C., Lee, B. H., D'Ambro, E. L., Kurtén, T., & Thornton, J. a. (2015).
 989 Constraining the sensitivity of iodide adduct chemical ionization mass spectrometry to multifunctional organic
 990 molecules using the collision limit and thermodynamic stability of iodide ion adducts. *Atmospheric*
 991 *Measurement Techniques Discussions*, 8(10), 10875–10896. <https://doi.org/10.5194/amtd-8-10875-2015>

992 Loubet, B., Buysse, P., Gonzaga-Gomez, L., Lafouge, F., Ciuraru, R., Decuq, C., et al. (2022). Volatile organic
 993 compound fluxes over a winter wheat field by PTR-Qi-TOF-MS and eddy covariance. *Atmospheric Chemistry*
 994 *and Physics*, 22(4), 2817–2842. <https://doi.org/10.5194/ACP-22-2817-2022>

995 Mattila, J. M., Brophy, P., Kirkland, J., Hall, S., Ullmann, K., Fischer, E. V., et al. (2018). Tropospheric sources and
 996 sinks of gas-phase acids in the Colorado Front Range. *Atmospheric Chemistry and Physics*, 18(16), 12315–
 997 12327. <https://doi.org/10.5194/ACP-18-12315-2018>

998 Mattila, J. M., Lakey, P. S. J., Shiraiwa, M., Wang, C., Abbatt, J. P. D., Arata, C., et al. (2020). Multiphase
 999 Chemistry Controls Inorganic Chlorinated and Nitrogenated Compounds in Indoor Air during Bleach
 1000 Cleaning. *Environmental Science and Technology*, 54(3), 1730–1739.
 1001 https://doi.org/10.1021/ACS.EST.9B05767/ASSET/IMAGES/MEDIUM/ES9B05767_M012.GIF

1002 Mauder, M., Cuntz, M., Drüe, C., Graf, A., Rebmann, C., Schmid, H. P., et al. (2013). A strategy for quality and
 1003 uncertainty assessment of long-term eddy-covariance measurements. *Agricultural and Forest Meteorology*,
 1004 169, 122–135. <https://doi.org/10.1016/J.AGRFORMET.2012.09.006>

1005 Mellouki, A., Wallington, T. J., & Chen, J. (2015). Atmospheric Chemistry of Oxygenated Volatile Organic
 1006 Compounds: Impacts on Air Quality and Climate. *Chemical Reviews*, 115(10), 3984–4014.
 1007 <https://doi.org/10.1021/cr500549n>

1008 Millet, D. B., Jacob, D. J., Custer, T. G., De Gouw, J. A., Goldstein, A. H., Karl, T., et al. (2008). New constraints
 1009 on terrestrial and oceanic sources of atmospheric methanol. *Atmospheric Chemistry and Physics*, 8(23), 6887–
 1010 6905. <https://doi.org/10.5194/acp-8-6887-2008>

1011 Millet, D. B., Baasandorj, M., Farmer, D. K., Thornton, J. A., Baumann, K., Brophy, P., et al. (2015). A large and
 1012 ubiquitous source of atmospheric formic acid. *Atmospheric Chemistry and Physics*, 15(11), 6283–6304.
 1013 <https://doi.org/10.5194/acp-15-6283-2015>

1014 Millet, D. B., Guenther, A., Siegel, D. A., Nelson, N. B., Singh, H. B., Gouw, J. A. De, et al. (2010). Global
 1015 atmospheric budget of acetaldehyde : 3-D model analysis and constraints from in-situ and satellite
 1016 observations. *Atmospheric Chemistry and Physics*, 10, 3405–3425.

1017 Millet, D. B., Alwe, H. D., Chen, X., Deventer, M. J., Griffis, T. J., Holzinger, R., et al. (2018). Bidirectional
 1018 Ecosystem-Atmosphere Fluxes of Volatile Organic Compounds Across the Mass Spectrum: How Many
 1019 Matter? *ACS Earth and Space Chemistry*, 2(8), 764–777. <https://doi.org/10.1021/acsearthspacechem.8b00061>

1020 Muller, J.-F., & Brasseur, G. (1999). Source of upper tropospheric HOx: A three-dimensional study. *Journal of*
 1021 *Geophysical Research*, 104, 1705–1715.

1022 Müller, M., Mikoviny, T., Jud, W., D’Anna, B., & Wisthaler, A. (2013). A new software tool for the analysis of high
 1023 resolution PTR-TOF mass spectra. *Chemometrics and Intelligent Laboratory Systems*, 127, 158–165.
 1024 <https://doi.org/10.1016/J.CHEMOLAB.2013.06.011>

1025 Nguyen, T. B., Crounse, J. D., Teng, A. P., St Clair, J. M., Paulot, F., Wolfe, G. M., & Wennberg, P. O. (2015).
 1026 Rapid deposition of oxidized biogenic compounds to a temperate forest. *Proceedings of the National Academy*
 1027 *of Sciences of the United States of America*, 112(5), E392–401. <https://doi.org/10.1073/pnas.1418702112>

1028 Olson, D. M., Dinerstein, E., Wikramanayake, E. D., Burgess, N. D., Powell, G. V. N., Underwood, E. C., et al.
 1029 (2001). Terrestrial ecoregions of the world: A new map of life on Earth. *BioScience*, 51(11), 933–938.
 1030 [https://doi.org/10.1641/0006-3568\(2001\)051\[0933:TEOTWA\]2.0.CO;2](https://doi.org/10.1641/0006-3568(2001)051[0933:TEOTWA]2.0.CO;2)

1031 Ortega, J., Turnipseed, A., Guenther, A. B., Karl, T. G., Day, D. A., Gochis, D., et al. (2014). Overview of the
 1032 Manitou experimental forest observatory: Site description and selected science results from 2008 to 2013.
 1033 *Atmospheric Chemistry and Physics*, 14(12), 6345–6367. <https://doi.org/10.5194/acp-14-6345-2014>

1034 Pagonis, D., Sekimoto, K., & de Gouw, J. (2019). A Library of Proton-Transfer Reactions of H₃O⁺ Ions Used for
 1035 Trace Gas Detection. *Journal of the American Society for Mass Spectrometry*, 30(7), 1330–1335.
 1036 https://doi.org/10.1007/S13361-019-02209-3/SUPPL_FILE/JS8B06050_SI_001.XLSX

1037 Park, J. H., Goldstein, A. H., Timkovsky, J., Fares, S., Weber, R., Karlik, J., & Holzinger, R. (2013). Active
 1038 atmosphere-ecosystem exchange of the vast majority of detected volatile organic compounds. *Science*,
 1039 341(6146), 643–647. <https://doi.org/10.1126/science.1235053>

1040 Philip, S., Martin, R. V., & Keller, C. A. (2016). Sensitivity of chemistry-transport model simulations to the duration
 1041 of chemical and transport operators: A case study with GEOS-Chem v10-01. *Geoscientific Model*
 1042 *Development*, 9(5), 1683–1695. <https://doi.org/10.5194/GMD-9-1683-2016>

1043 Reissell, A., Arey, J., & Atkinson, R. (2000). Atmospheric Chemistry of Camphor. *Int J Chem Kinet*, 33, 56–63.
 1044 <https://doi.org/10.1002/1097-4601>

1045 Rhew, R. C., Deventer, M. J., Turnipseed, A. A., Warneke, C., Ortega, J., Shen, S., et al. (2017). Ethene, propene,
 1046 butene and isoprene emissions from a ponderosa pine forest measured by relaxed eddy accumulation.
 1047 *Atmospheric Chemistry and Physics*, 17(21), 13417–13438. <https://doi.org/10.5194/acp-17-13417-2017>

1048 Riches, M., Lee, D., & Farmer, D. K. (2020). Simultaneous leaf-level measurement of trace gas emissions and
 1049 photosynthesis with a portable photosynthesis system. *Atmospheric Measurement Techniques*, 13(8), 4123–
 1050 4139. <https://doi.org/10.5194/AMT-13-4123-2020>

1051 Richters, S., Herrmann, H., & Berndt, T. (2015). Gas-phase rate coefficients of the reaction of ozone with four
 1052 sesquiterpenes at 295 ± 2 K. *Physical Chemistry Chemical Physics*, 17(17), 11658–11669.
 1053 <https://doi.org/10.1039/c4cp05542j>

1054 Riva, M., Rantala, P., Krechmer, J. E., Peräkylä, O., Zhang, Y., Heikkinen, L., et al. (2018). Evaluating the
 1055 performance of five different chemical ionization techniques for detecting gaseous oxygenated organic
 1056 species. *Atmospheric Measurement Techniques Discussions*, 1–39. <https://doi.org/10.5194/amt-2018-407>

1057 Safieddine, S. A., Heald, C. L., & Henderson, B. H. (2017). The global nonmethane reactive organic carbon budget:
 1058 A modeling perspective. *Geophysical Research Letters*, 44(8), 3897–3906.
 1059 <https://doi.org/10.1002/2017GL072602>

1060 Sander, R. (2015). Compilation of Henry’s law constants (version 4.0) for water as solvent. *Atmospheric Chemistry*
 1061 *and Physics*, 15(8), 4399–4981. <https://doi.org/10.5194/acp-15-4399-2015>

- Saunders, S. M., Jenkin, M. E., Derwent, R. G., & Pilling, M. J. (2003). Protocol for the development of the Master Chemical Mechanism, MCM v3 (Part A): Tropospheric degradation of non-aromatic volatile organic compounds. *Atmospheric Chemistry and Physics*, 3(1), 161–180. <https://doi.org/10.5194/acp-3-161-2003>
- Schade, G. W., Goldstein, A. H., & Lamanna, M. S. (1999). Are Monoterpene Emissions influenced by Humidity? *Geophysical Research Letters*, 26(14), 2187–2190. <https://doi.org/10.1029/1999GL900444>
- Sindelarova, K., Granier, C., Bouarar, I., Guenther, A., Tilmes, S., Stavrakou, T., et al. (2014). Global data set of biogenic VOC emissions calculated by the MEGAN model over the last 30 years. *Atmospheric Chemistry and Physics*, 14(17), 9317–9341. <https://doi.org/10.5194/acp-14-9317-2014>
- Singh, H. B., Kanakidou, M., Crutzen, P. J., & Jacob, D. J. (1995). High concentrations and photochemical fate of oxygenated hydrocarbons in the global troposphere. *Nature*, 378(6552), 50–54. <https://doi.org/10.1038/378050a0>
- Stedman, D. H., & Niki, H. (1973). Ozonolysis Rates of Some Atmospheric Gases. <http://Dx.Doi.Org/10.1080/00139307309435501>, 4(4), 303–310. <https://doi.org/10.1080/00139307309435501>
- Stull, R. B. (1988). *An Introduction to Boundary Layer Meteorology*.
- Tomaz, S., Cui, T., Chen, Y., Sexton, K. G., Roberts, J. M., Warneke, C., et al. (2018). Photochemical Cloud Processing of Primary Wildfire Emissions as a Potential Source of Secondary Organic Aerosol. *Environmental Science and Technology*, 52(19), 11027–11037. <https://doi.org/10.1021/ACS.EST.8B03293> ASSET/IMAGES/LARGE/ES-2018-032933_0004.JPEG
- Tsiligiannis, E., Wu, R., Lee, B. H., Salvador, C. M., Priestley, M., Carlsson, P. T. M., et al. (2022). A Four Carbon Organonitrate as a Significant Product of Secondary Isoprene Chemistry. *Geophysical Research Letters*, 49(11), e2021GL097366. <https://doi.org/10.1029/2021GL097366>
- Vermeuel, M. P., Novak, G. A., Kilgour, D. B., Claflin, M. S., Lerner, B. M., Trowbridge, A. M., et al. (2022). Observations of biogenic volatile organic compounds over a mixed temperate forest during the summer to autumn transition. *Atmospheric Chemistry and Physics Discussions*. <https://doi.org/https://doi.org/10.5194/egusphere-2022-1015>
- Wang, X., Jacob, D. J., Eastham, S. D., Sulprizio, M. P., Zhu, L., Chen, Q., et al. (2019). The role of chlorine in global tropospheric chemistry. *Atmospheric Chemistry and Physics*, 19(6), 3981–4003. <https://doi.org/10.5194/ACP-19-3981-2019>
- Wolfe, G. M., Cantrell, C., Kim, S., Mauldin, R. L., Karl, T., Harley, P., et al. (2014). Missing peroxy radical sources within a summertime ponderosa pine forest. *Atmospheric Chemistry and Physics*, 14(9), 4715–4732. <https://doi.org/10.5194/acp-14-4715-2014>
- Yáñez-Serrano, A. M., Nölscher, A. C., Williams, J., Wolff, S., Alves, E., Martins, G. A., et al. (2015). Diel and seasonal changes of biogenic volatile organic compounds within and above an Amazonian rainforest. *Atmospheric Chemistry and Physics*, 15(6), 3359–3378. <https://doi.org/10.5194/acp-15-3359-2015>
- Yuan, B., Koss, A. R., Warneke, C., Coggon, M., Sekimoto, K., & De Gouw, J. A. (2017). Proton-Transfer-Reaction Mass Spectrometry: Applications in Atmospheric Sciences. *Chemical Reviews*, 117(21), 13187–13229. <https://doi.org/10.1021/ACS.CHEMREV.7B00325> SUPPL_FILE/CR7B00325_SI_001.PDF
- Zhou, L., Gierens, R., Sogachev, A., Mogensen, D., Ortega, J., Smith, J. N., et al. (2015). Contribution from biogenic organic compounds to particle growth during the 2010 BEACHON-ROCS campaign in a Colorado temperate needleleaf forest. *Atmospheric Chemistry and Physics*, 15(15), 8643–8656. <https://doi.org/10.5194/acp-15-8643-2015>